



**HAL**  
open science

## The molecular gas resolved by ALMA in the low-metallicity merging dwarf galaxy Haro 11

Yulong Gao, Qiusheng Gu, Yong Shi, Luwenjia Zhou, Min Bao, Xiaoling Yu, Zhiyu Zhang, Tao Wang, Suzanne C. Madden, Matthew Hayes, et al.

► **To cite this version:**

Yulong Gao, Qiusheng Gu, Yong Shi, Luwenjia Zhou, Min Bao, et al.. The molecular gas resolved by ALMA in the low-metallicity merging dwarf galaxy Haro 11. *Astronomy & Astrophysics - A&A*, 2022, 661, pp.A136. 10.1051/0004-6361/202142309 . hal-03595478

**HAL Id: hal-03595478**


**<https://hal.science/hal-03595478v1>**

Submitted on 18 Mar 2023

**HAL** is a multi-disciplinary open access archive for the deposit and dissemination of scientific research documents, whether they are published or not. The documents may come from teaching and research institutions in France or abroad, or from public or private research centers.

L'archive ouverte pluridisciplinaire **HAL**, est destinée au dépôt et à la diffusion de documents scientifiques de niveau recherche, publiés ou non, émanant des établissements d'enseignement et de recherche français ou étrangers, des laboratoires publics ou privés.

# The molecular gas resolved by ALMA in the low-metallicity merging dwarf galaxy Haro 11

Yulong Gao (高玉龙)<sup>1,2</sup> , Qiusheng Gu (顾秋生)<sup>1,2</sup>, Yong Shi<sup>1,2</sup>, Luwenjia Zhou<sup>1,2</sup>,  
Min Bao<sup>1,3,4</sup>, Xiaoling Yu<sup>1,2</sup>, Zhi-Yu Zhang<sup>1,2</sup>, Tao Wang<sup>1,2</sup>, Suzanne C. Madden<sup>5</sup>, Matthew Hayes<sup>6</sup>,  
Shiying Lu<sup>1,2</sup>, and Ke Xu<sup>1,2</sup>

<sup>1</sup> School of Astronomy and Space Science, Nanjing University, Nanjing 210093, PR China  
e-mail: yulong@nju.edu.cn

<sup>2</sup> Key Laboratory of Modern Astronomy and Astrophysics (Nanjing University), Ministry of Education, Nanjing 210093, PR China

<sup>3</sup> School of Physics and Technology, Nanjing Normal University, Nanjing 210023, PR China

<sup>4</sup> Institute of Astronomy, The University of Tokyo, Osawa 2-21-1, Mitaka, Tokyo 181-0015, Japan

<sup>5</sup> CEA, Irfu, DAp, AIM, Université Paris-Saclay, Université de Paris, CNRS, 91191 Gif-sur-Yvette, France

<sup>6</sup> Stockholm University, Department of Astronomy and Oskar Klein Centre for Cosmoparticle Physics, AlbaNova University Centre, SE 10691, Stockholm, Sweden

Received 27 September 2021 / Accepted 11 February 2022

## ABSTRACT

**Context.** The physical mechanisms driving starbursts and quenching in less massive ( $M_* \leq 10^{10} M_\odot$ ) galaxies are unclear. The merger is one of the inescapable processes referred to as both starburst and quenching in massive galaxies. However, the effects of the merger on star formation in dwarf galaxies and their evolution are still uncertain.

**Aims.** We aim to explore how star formation in dwarf galaxies is both triggered and quenched by studying metal-poor gas-rich dwarf mergers based on multi-band observations at a spatial resolution of  $\sim 460$  pc.

**Methods.** We use archival data of Atacama Large Millimetre Array (Band 3 and 8) and Very Large Telescope/Multi Unit Spectroscopic Explorer to map CO( $J = 1-0$ ), [CI]( $^3P_1-^3P_0$ ), and H $\alpha$  emission in one of the most extreme merging starburst dwarf galaxies, Haro 11.

**Results.** We find the molecular gas is assembled around the central two star-forming regions (knots B and C). The molecular and ionized gas and stellar components show complex kinematics, indicating that the gas is probably at a combined stage of collision of clouds and feedback from star formation. The peak location and distribution of [CI](1-0) closely coincide with the CO(1-0) emission, meaning that it might trace the same molecular gas as CO in such a dwarf merger starburst galaxy. The enhancement of line ratios ( $\sim 0.5$ ) of [CI]/CO around knot C is probably generated by the dissociation of CO molecules by cosmic rays and far-ultraviolet photons. Globally, Haro 11 and its star-forming regions share similar star formation efficiency (SFE) to the high- $z$  starburst galaxies or the clumps in nearby ultraluminous infrared galaxies.

**Conclusions.** Given the high SFE, the high specific star formation rate, small stellar mass, low metallicity, and deficient HI gas, Haro 11 could be an analog of a high- $z$  dwarf starburst and the potential progenitor of the nearby less massive elliptical galaxies. The significantly smaller turbulent pressure and virial parameter is probably triggering the intense starbursts. We predict that Haro 11 will quench at  $M_* \leq 8.5 \times 10^9 M_\odot$ .

**Key words.** galaxies: ISM – galaxies: starburst – galaxies: individual: Haro 11 – galaxies: interactions

## 1. Introduction

The physical causes of starburst and quenching of galaxies are open questions. In the star formation rate (SFR) versus stellar mass ( $M_*$ ) space, galaxies can be separated into two broad categories. Star-forming galaxies (SFGs, also known as blue clouds), most of which are spiral or late-type galaxies, lie on an almost linear relation between the stellar mass and SFR called the main sequence (Brinchmann et al. 2004; Daddi et al. 2007; Peng et al. 2010; Lilly et al. 2013; Speagle et al. 2014). Starburst galaxies undergo an exceptionally intense evolutionary phase of star formation during their lifetime, and are located above the main sequence (Elbaz et al. 2018; Orlitova 2020). Quiescent galaxies (QGs, or “red sequences”), which is most elliptical or early-type galaxies, have a significantly lower SFR than SFGs and thus lie below the main sequence. Some so-called “green valley” galaxies lie between the blue SFGs and red QGs, and have been

regraded as the transition zone or quenching galaxies (Bell et al. 2003; Fang et al. 2012). The existence of these galaxies above and below the main sequence implies that SFGs might enhance or shut down their star formation at some point during their lifetime.

A variety of processes can induce starburst activities in galaxies. The strong tidal force caused by gravitational interactions between close pairs or merger galaxies will perturb the orbits of gas and stars, triggering efficient gas flow toward the galaxy centers (Larson & Tinsley 1978; Di Matteo et al. 2007; Ellison et al. 2008). In spiral-barred galaxies, because of the gravitational instabilities of the stellar bar, the gas in the outer spiral can also be transferred into the central region and form new stars (Hopkins & Quataert 2010; Elmegreen et al. 2009; Emsellem et al. 2015; Díaz-García et al. 2021). Similarly, star formation quenching is correlated with active galactic nucleus (AGN) feedback (Di Matteo et al. 2005; Kauffmann et al. 2007;

Fabian 2012; Cheung et al. 2016; Kaviraj et al. 2017; Chen et al. 2022; He et al. 2019, 2022) and secular processes, such as stellar bars, oval disks, and spiral structures (Kormendy et al. 2004; Masters et al. 2011; Cheung et al. 2013). Meanwhile, some external processes, such as the galaxy environment and major mergers (Di Matteo et al. 2005; Hopkins et al. 2006, 2008; Knobel et al. 2015; Peng et al. 2015; Weigel et al. 2017), can also affect gas consumption and lead to the quenching of star formation.

The merging of galaxies is one of the inescapable processes in galaxy evolution, for both the starburst and quenching activities (Hopkins & Quataert 2010). By perturbing gas rotation, mergers lead to the rapid inflow of gas and power the intense starburst or feed the central massive black hole. Energetic feedback from AGNs or starbursts heats the interstellar medium (ISM), preventing the gas from cooling and sweeps out gas from the host galaxy (Fabian 2012; Cheung et al. 2016; Harrison et al. 2018), which suppresses star formation and converts the blue SFGs into quiescent red massive elliptical galaxies. In the local Universe, major mergers are always observed between spiral galaxies, which could result in the ultraluminous infrared galaxies ((U)LIRGs; Papadopoulos et al. 2007; Israel et al. 2015; Espada et al. 2018; Spence et al. 2018; Shangguan et al. 2019). In the high-redshift Universe, where galaxy mergers are more prevalent, most of the observed merger cases are bright and massive submillimeter galaxies (SMGs; Alexander et al. 2005; Shapiro et al. 2008; Narayanan et al. 2010; Brisbin et al. 2017; Wardlow et al. 2017), which have been suggested to be the progenitors of massive quiescent elliptical galaxies in the local Universe.

However, the mechanisms of triggering and quenching star formation in low stellar mass or dwarf galaxies ( $M_* < 5 \times 10^9 M_\odot$ , Stierwalt et al. 2015) are unclear. While a large fraction (>70%) of the galaxies in the local Universe are dwarfs, only a few percent of them are starburst galaxies, including blue compact galaxies (BCGs), Lyman- $\alpha$  reference sample (LARS, Hayes et al. 2013; Östlin et al. 2014), Lyman-break analogs (LBAs, Heckman et al. 2001, 2005), and Green Peas (see the review in Orlitova 2020). Many BCGs are relatively isolated, while the morphologies and velocity distribution suggest a recent interaction with neighbors. Furthermore, the stellar components in BCGs contain a mixture of young and old populations (Kunth & Östlin 2000), perhaps indicating that interactions are responsible for the starburst activity in BCGs. However, because of the weak gravitational potential and strong turbulence of stellar winds, the conversion from molecular gas to stars is suggested to be inefficient based on previous star formation models. Whether or not the merging of two dwarf galaxies can trigger starburst activity is still an open question. Recently, Zhang et al. (2020a,b) reported that the star cluster formation rate ( $\propto$ SFR) in the galaxy VCC 848, a remnant of a gas-rich dwarf–dwarf merger, is enhanced by  $\sim 1.0$  dex during the past  $\sim 1$  Gyr relative to its earlier times.

Although dwarf–dwarf mergers are relatively rare ( $\sim 3\%$ , Kado-Fong et al. 2020) between dwarf galaxies in the local Universe, they are expected to be frequent at high redshift (Fensch et al. 2017; Huško et al. 2022; Romano et al. 2021; Whitney et al. 2021). The evolution of these dwarf mergers is still uncertain. Geha et al. (2012) performed a systematic study of the quenched field galaxy fraction using the SDSS DR8 spectra, demonstrating that it is smaller than 0.06% when  $M_* < 10^9 M_\odot$ , but is about 0.5% and 3% for less massive galaxies at  $M_* < 10^{9.5} M_\odot$  and  $M_* < 10^{9.9} M_\odot$ , respectively. Assuming the merger quenching scenario in dwarf galaxies is similar to that of more massive ones, dwarf mergers at high redshift would be

the progenitors of these nearby dwarf elliptical galaxies. However, it is difficult to study the detailed starburst activities and gas consumption for these distant dwarf mergers because of the low brightness. Thus, for analogs of these distant cases, metal-poor gas-rich dwarf mergers with high spatial resolution, multi-band observations can provide ideal laboratories to study the physical mechanisms of triggering and quenching of star formation in such dwarf galaxies.

In this paper, we focus on the molecular and neutral gas properties of Haro 11, which is a merging system and one of the most extreme starburst BCDs in the nearby Universe (Cormier et al. 2012, 2014; Östlin et al. 2015, 2021; Pardy et al. 2016; Menacho et al. 2019, 2021). The redshift ( $z$ ) is about 0.0206, collected from the NASA/IPAC Extragalactic Database<sup>1</sup> (NED), corresponding to a distance of 87.2 Mpc and a scale of 420 pc per arcsecond. Haro 11 is a late-stage merger, showing similar morphology and kinematics of stars and ionized gas to the well-known Antennae (NGC 4038/4039) galaxy (Östlin et al. 2015). The starburst activities mainly occur at three bright knots: labeled A (south-western), B (central), and C (eastern), shown in Fig. 1. These knots are found to contain more than 200 massive star clusters (Adamo et al. 2010; Östlin et al. 2015; Menacho et al. 2021). Stellar feedback produced by intense starbursts has created outflows and multi-scale structures, such as filaments, arcs, and bubbles, which make the merger kinematics much more complex (Menacho et al. 2021). The gas-phase metallicities ( $12 + \log(\text{O}/\text{H})$ ,  $Z$ ), calculated from the electron temperature method, are about 8.09 ( $0.24 Z_\odot$ ), 8.25 ( $0.35 Z_\odot$ ) and 7.80 ( $0.12 Z_\odot$ ) for knots A, B, and C, respectively (James et al. 2013). The total SFR is about  $25.1^{+28.6}_{-13.4} M_\odot \text{ yr}^{-1}$  based on the  $\text{H}\alpha$  and infrared luminosity (Rémy-Ruyer et al. 2015). The molecular gas tracers CO(1–0), CO(2–1), and CO(3–2) detected by ATNF Mopra 22-m and APEX telescopes determined that the total  $\text{H}_2$  gas mass ranges from  $2.5 \times 10^8 M_\odot$  using a Galactic conversion factor,  $X_{\text{CO}}$  (Cormier et al. 2014). The dust mass derived from the dust spectral energy distribution modeling of the mid-infrared to submillimeter observations, which included *Spitzer* and *Herschel* data, is  $9.9 \times 10^6 M_\odot$  (Rémy-Ruyer et al. 2015). Pardy et al. (2016) presented the first robust detection of HI 21 cm emission for Haro 11 using the GBT telescope, and found the HI mass to be about  $5.1 \times 10^8 M_\odot$ . Cormier et al. (2014) and Pardy et al. (2016) reported that the gas in Haro 11 is dominated by molecular gas instead of HI gas. Cormier et al. (2014) also found the gas depletion of Haro 11 is very rapid, about 0.1 Gyr, indicating that it is efficient in forming stars. However, the presence of additional molecular gas not traced by CO (CO-dark molecular gas) proposed by Madden et al. (2020), reduces the SFR efficiency.

However, limited by the large beam size of the single antenna in previous studies, we cannot answer the questions of: what the distribution of molecular gas in Haro 11 is; what conditions within these individual gas clouds encourage the presence of starbursts; how star formation efficiency (SFE) varies within the galaxy; how the gas depletion compares to the star-forming regions in massive merger systems, for example (U)LIRGs; what the role of different gas phases in such a dwarf merger system is; what the impact of the starburst is on the surrounding molecular and atomic gas; and how the conversion from HI to  $\text{H}_2$  in the dwarf mergers compares to massive mergers and other isolated galaxies. To address these questions, we collected and analyzed high-resolution sub/millimeter Atacama Large Millimetre Array (ALMA) observations of CO( $J = 1-0$ ) (hereafter CO(1–0)) and

<sup>1</sup> <http://ned.ipac.caltech.edu>

[CI]( $^3P_1-^3P_0$ ) (hereafter [CI](1–0)) emission lines and archival optical Very Large Telescope (VLT)/Multi Unit Spectroscopic Explorer (MUSE) data, to investigate the starburst activities and gas consumption in Haro 11 at 500 pc scales.

The organization of the present paper is as follows: In Sect. 2, we present the observations and data reduction, and then derive the properties of the molecular gas and star formation activities. The main results and comparison with other galaxies are presented in Sects. 3 and 4, respectively, and a summary is given in Sect. 5. Throughout the paper, we assume a flat  $\Lambda$ CDM cosmology model,  $\Omega_\Lambda = 0.7$ ,  $\Omega_m = 0.3$ , and  $H_0 = 70 \text{ km s}^{-1} \text{ Mpc}^{-1}$ . We adopt the solar metallicity ( $Z_\odot$ ) as  $12 + \log(\text{O}/\text{H}) = 8.69$  (Allende Prieto et al. 2001).

## 2. Observations and data reduction

### 2.1. ALMA data

For this study, we collected the band 3 and band 8 observations (ID: 2013.1.00350.S, PI: Cormier; 2017.1.01457.S, PI: Hayes) from the ALMA data archive. The band 3 observations (12-m array) were obtained on 7 August 2016, with a total integration time of 2903 s and a field of view (FoV) of  $\sim 55''$ . The frequency ranges from 112.0 to 113.8 GHz, covering the CO(1–0) emission line. The longer integration time (8981 s) observations in band 8 (12-m array) were performed on 13 May 2018, covering an FoV of  $\sim 12''$ . The frequency (481–483 GHz) covers the [CI](1–0) emission line. The largest angular scales are about  $4.2''$  and  $5.3''$  for band 3 and band 8 observations, respectively. We use the Common Astronomy Software Applications (CASA) package (version 5.7, McMullin et al. 2007) to perform the standard calibration. The ALMA data were cleaned with the natural weighting with the CASA task *tclean* and were primary-beam corrected. The synthesized beam sizes in the CO(1–0) and [CI](1–0) final data cubes are about  $1.1'' \times 1.0''$  ( $462 \times 420 \text{ pc}$ ) and  $0.5'' \times 0.5''$  ( $\times 210 \text{ pc}$ ), respectively. The pixel sizes in CO and [CI] images are about  $0.1''$ . The rms values are about  $1.2 \text{ mJy/beam}^{-1}$  and  $1.3 \text{ mJy/beam}^{-1}$  for CO(1–0) and [CI](1–0) data at a channel width of  $5 \text{ km s}^{-1}$ , respectively. We create the CO and [CI] moment maps with the CASA task *immo-*  
*ments* by applying a threshold of four times the rms.

### 2.2. VLT/MUSE data

Haro 11 was observed by VLT/MUSE (Bacon et al. 2010) on December 2014 and August 2016 (Menacho et al. 2019, 2021). The integration exposure time at the central  $30'' \times 30''$  region is about 3.1 h. We collect the fully reduced data cube from the ESO archive website<sup>2</sup>. The seeing values during the observations are  $0.6-0.9''$ , and the FWHM of the final image is about  $0.8''$  (Menacho et al. 2019). The rest-frame spectral range is  $4750-9160 \text{ \AA}$  with a channel width of  $1.25 \text{ \AA}$ .

We used the STARLIGHT package to reproduce the stellar continuum in order to derive the flux of pure emission lines (Cid Fernandes et al. 2005). In this process, we assumed the Chabrier (2003) initial mass function (IMF), and performed a combination of 45 single stellar populations (SSPs) from the Bruzual & Charlot (2003) model, which consists of three different metallicities and 15 stellar ages. The stellar mass within each spatial pixel can be derived from the SSP fitting results with an uncertainty of 0.11 dex (Bruzual & Charlot 2003; Cid Fernandes et al. 2005). The total stellar mass was estimated

by integrating the values in each pixel with continuum S/N larger than 5.0, and then converting to the Kroupa (2001) IMF by adding 0.15 dex (Bell et al. 2003; Shangguan et al. 2019). After subtracting the stellar continuum synthesis, we applied multiple Gaussians to fit these strong emission lines, such as H $\alpha$ , H $\beta$ , and [O III] $\lambda\lambda 4959, 5007$ .

### 2.3. Star formation knots

We can resolve Haro 11 into smaller star formation knots with high-spatial-resolution images from ALMA and MUSE. We used the Python package *Astrodendro*<sup>3</sup> (Goodman et al. 2009) to search for star-forming clumps in the H $\alpha$  map. This clump-finding algorithm is based on the dendrogram and has been used to identify reliable star-forming cores in galaxies (see Li et al. 2020 for the detailed comparison of different clump-finding packages). To define the boundaries of clump structures, we can specify a few parameters: *min\_value*, *min\_delta* and *min\_npix*. The *min\_value* constrains the minimum value in the field to be considered, *min\_delta* represents the minimum significance of the structure to avoid including local maxima, and *min\_npix* specifies the minimum number of pixels that a structure should contain. We assumed a *min\_npix* of 16. The identified knots are shown in Fig. 1, in which A, B, and C are same as in previous studies Adamo et al. (2010), Östlin et al. (2015), Menacho et al. (2021). Furthermore, the smaller star formation knot T (the name is the same as in Table 3 of Vader et al. 1993), containing young massive star clusters, is also marked in Fig. 1 and is referred to as the ear between knots A and B (Östlin et al. 2015; Table 1).

## 3. Results

The spatial distribution of ionized and molecular gas can provide essential information about the gas kinematics and star formation activity. Here we describe the spatial distribution of the molecular gas within Haro 11 for the first time and investigate the gas depletion and star formation processes for the individual starburst regions.

### 3.1. Measurements of molecular gas mass and star formation rate

We use the CO(1–0) integrated intensity to derive the molecular gas mass, following the relation in Bolatto et al. (2013):

$$M_{\text{H}_2} = \alpha_{\text{CO}} \times L_{\text{CO}}, \quad (1)$$

where  $M_{\text{H}_2}$  is the molecular gas mass in units of solar mass, and  $L_{\text{CO}}$  is the luminosity of CO(1–0) emission in units of  $\text{K km s}^{-1} \text{ pc}^2$ .  $L_{\text{CO}}$  can be derived using the following equation:

$$L_{\text{CO}} = 2453 \times I_{\text{CO}} \times D_L^2 / (1 + z), \quad (2)$$

where  $I_{\text{CO}}$  is the integrated flux in  $\text{Jy km s}^{-1}$ ,  $D_L$  is the luminosity distance (Mpc), and the redshift ( $z$ ) is adopted as 0.0206467 (Menacho et al. 2019). The conversion factor  $\alpha_{\text{CO}}$  is dependent on the gas-phase metallicity (Bolatto et al. 2013; Hunt et al. 2014; Shi et al. 2016). James et al. (2013) and Menacho et al. (2021) mentioned the variations in spatially resolved oxygen abundances between electron temperature method and strong emission line diagnoses (Marino et al. 2013)

<sup>2</sup> <http://archive.eso.org/scienceportal/home>

<sup>3</sup> <https://dendrograms.readthedocs.io/en/stable/>



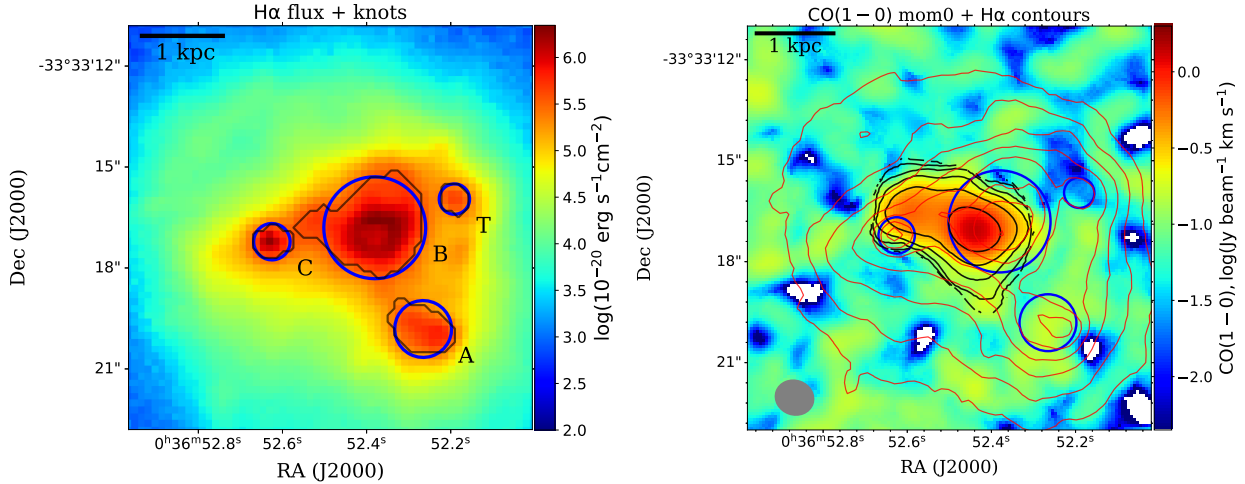


**Fig. 1.** Emission distribution of ionized and molecular gas in Haro 11. *Left* integrated intensity map of attenuation-corrected  $H\alpha$  emission. The gray contours represent the identified star formation knots by *Astrodedro*, and the blue circles show the same area size. *Right* integrated intensity (moment 0) of the CO(1–0) emission line without threshold setting. The black contours represent the integrated intensity of CO(1–0) with a  $4 \times$  rms threshold. The  $H\alpha$  intensity is marked by red contours, with levels of  $(1/2)^n$  ( $n = 1, 2, \dots, 8$ ) times the maximum value of  $H\alpha$  intensity. The CO(1–0) beam size is shown as a solid gray elliptical circle in the bottom left.

**Table 1.** Properties of star formation knots

Property	RA (J2000)	Dec (J2000)	Diameter	$12 + \log(\text{O}/\text{H})$	$M_*$	SFR	$M_{\text{H}_2}$	$\sigma_v$	$P_{\text{turb}}$	$\alpha_{\text{vir}}$
...	(deg)	(deg)	(arcsec (pc))	...	( $10^7 M_\odot$ )	( $M_\odot \text{ yr}^{-1}$ )	( $10^8 M_\odot$ )	( $\text{km s}^{-1}$ )	( $10^6 \text{ K cm}^{-3}$ )	...
A	9.2177732	-33.555504	1.7 (710.7)	$8.09 \pm 0.20$	$4.3 \pm 1.2$	$1.42 \pm 0.03$	$< 2.3$	...	...	...
B	9.2182527	-33.554668	3.0 (1254.2)	$8.25 \pm 0.15$	$8.9 \pm 2.6$	$10.92 \pm 0.08$	$23^{+20}_{-19}$	$23.8^{+3.7}_{-12.1}$	$8.7^{+16.9}_{-8.1}$	$0.17^{+0.17}_{-0.06}$
C	9.2192717	-33.554783	1.1 (459.8)	$7.80 \pm 0.13$	$19.1 \pm 5.5$	$1.09 \pm 0.02$	$1.1^{+1.0}_{-0.9}$	$16.2^{+6.6}_{-10.8}$	$1.7^{+4.0}_{-1.1}$	$0.15^{+0.09}_{-0.11}$
T	9.2174637	-33.554432	0.9 (376.3)	...	$0.3 \pm 0.1$	$0.31 \pm 0.02$	$< 0.1$	...	...	...

**Notes.** The metallicities ( $12 + \log(\text{O}/\text{H})$ ) were determined with the electron temperature method using the  $[\text{O III}]\lambda 4363$  emission line collected from [James et al. \(2013\)](#). The CO(1–0) velocity dispersion  $\sigma_v$ , internal turbulent pressure  $P_{\text{turb}}$ , and the virial parameter  $\alpha_{\text{vir}}$  are shown as median values and one-sigma ranges, respectively.

in Haro 11. Here, we select the temperature-based metallicities in [James et al. \(2013\)](#) and adopt the area-size-weighted average metallicity value of  $12 + \log(\text{O}/\text{H}) \sim 8.12$ . According to the metallicity– $\alpha_{\text{CO}}$  relation of [Shi et al. \(2016\)](#), we assume the average  $\alpha_{\text{CO}}$  of  $60 M_\odot (\text{K km s}^{-1} \text{ pc}^{-2})^{-1}$ , with a range of  $10\text{--}110 M_\odot (\text{K km s}^{-1} \text{ pc}^{-2})^{-1}$ . We calculate the gas mass uncertainty by considering the  $\alpha_{\text{CO}}$  range and three times the CO intensity rms. We then divide the molecular gas mass by the area size to compute the gas mass surface density  $\Sigma_{\text{H}_2}$ . Adopting the CO velocity width as  $200 \text{ km s}^{-1}$ , the  $\Sigma_{\text{H}_2}$  at four times the rms threshold is about  $2.3 \times 10^8 M_\odot \text{ kpc}^{-2}$ .

Based on the “Case B” recombination model and the [Calzetti et al. \(2000\)](#) reddening formalism, we obtained the extinction-corrected  $H\alpha$  flux using the  $H\alpha/H\beta$  ratio. According to the [Kroupa \(2001\)](#) IMF and the calibration relation in [Kennicutt \(1998\)](#),

$$\text{SFR}(M_\odot \text{ yr}^{-1}) = 7.92 \times 10^{-42} \times L_{\text{cor}}(H\alpha) (\text{erg s}^{-1}), \quad (3)$$

and the SFR can be determined from the  $H\alpha$  luminosity,  $L_{\text{cor}}(H\alpha)$ . The SFR uncertainty is computed from the  $H\alpha$  luminosity and attenuation uncertainties, which include the  $H\beta$  intensity errors. As most of the star formation in galaxies is discrete, [da Silva et al. \(2014\)](#) reported that different SFR tracers could produce large stochastic fluctuation ( $\geq 0.5$  dex) at the lowest SFR regimes. However, the uncertainty is negligible at a SFR higher than  $1 M_\odot \text{ yr}^{-1}$  ([da Silva et al. 2014](#)). Furthermore, the intrinsic SFR might be variable on shorter timescales in a merging

or interacting galaxy. The ionization-based tracers (such as  $H\alpha$ ) are preferable because we focus on the intense starburst regions in Haro 11, which have high SFR ( $\geq 1 M_\odot \text{ yr}^{-1}$ ). We compute the SFR surface density,  $\Sigma_{\text{SFR}}$ , taking into account the area of the regions.

### 3.2. CO(1–0) distribution and kinematics

In the left panel of [Fig. 1](#), we show the integrated intensity map of  $H\alpha$  emission. The star-forming knots (A, B, C, and T) identified in [Sect. 2.3](#) are marked as gray contours. The corresponding circular regions with equal areas are shown with blue circles. We used these circle regions in the subsequent analysis. A large fraction ( $\sim 44\%$ ) of SF is occurring within knot B. In the right panel, we present the integrated CO(1–0) intensity (moment 0) distribution contoured by  $H\alpha$  flux. The knots are also marked as blue circles. We note that molecular gas is concentrated around knots B and C, which contain about 55% and 4% of the gas mass, respectively. We also detect an offset between the CO and  $H\alpha$  intensity peaks, indicating the delay between compression of molecular gas and current star formation. The rest of the gas is distributed between knots B and C. No CO is detected at a significant level toward knots A and T. Furthermore, it seems that the star formation regions surround the remaining molecular gas, which might indicate two possible scenarios. One is that we did not detect the molecular gas associated with the recent star formation traced by  $H\alpha$  emission. Another is that the early-stage star formation

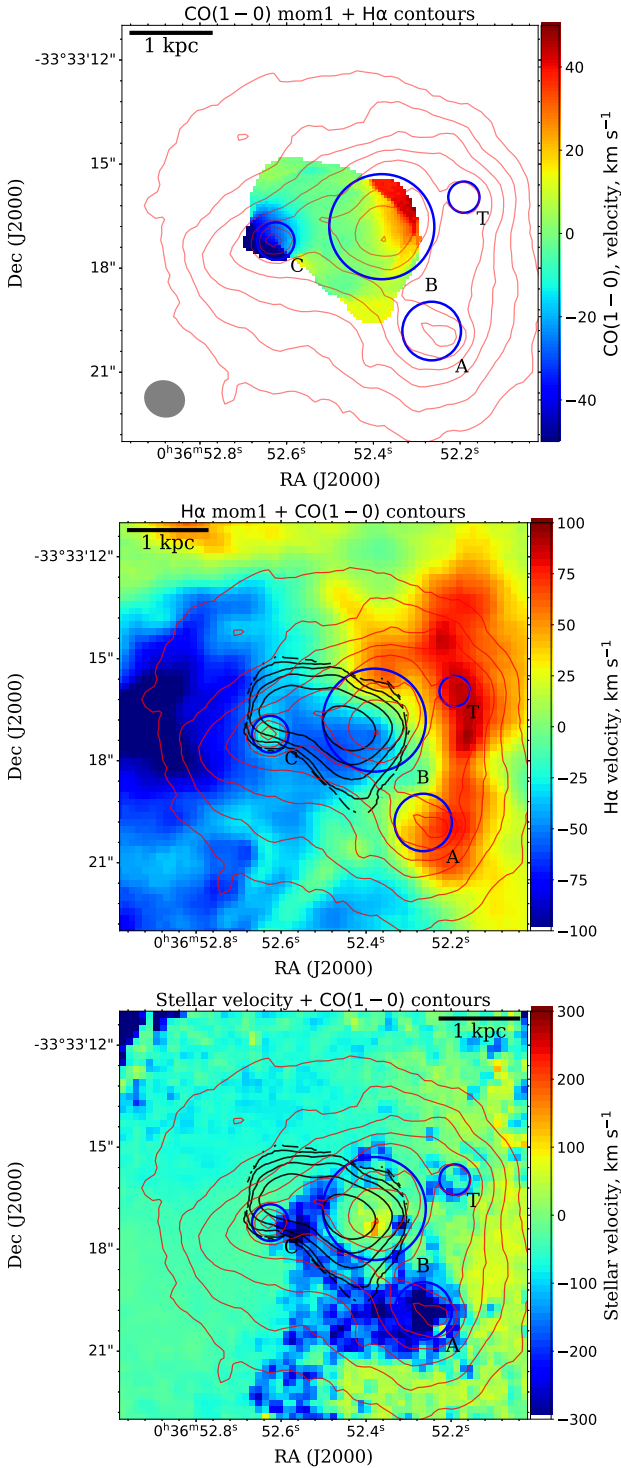


**Fig. 2.** Velocity distribution of molecular and ionized gas, as well as the stellar components, in Haro 11. *Top:* Systemic-velocity-subtracted intensity-weighted velocity field (moment 1,  $4 \times \text{rms}$ ) of CO(1–0) emission line. *Middle:* systemic velocity-subtracted intensity-weighted velocity field of H $\alpha$  emission. *Bottom:* Stellar velocity map derived from the SSP fitting results. Black contours and red contours represent the intensities of CO(1–0) and H $\alpha$  emission lines, respectively.

occurs within the CO peak, probably surrounded by dusty ISM, and thus the H $\alpha$  emission is not yet luminous.

The systemic velocity ( $V_{\text{sys}}$ ) of CO molecular gas in Haro 11 is estimated to be  $6051.3 \pm 2.1 \text{ km s}^{-1}$ . Figure 2 shows the

intensity-weighted velocity field (moment 1,  $V_{\text{obs}} - V_{\text{sys}}$ ) map of CO(1–0) and H $\alpha$  emission, as well as the velocity map of stellar components derived from the SSP fitting results. The H $\alpha$  flux contours are also overlaid on these panels, helping to visualize the spatial association between the molecular gas and star formation regions. The velocity distribution of CO(1–0) is approximately symmetric around the stellar center. The gas around the eastern region C is approaching, while the western side of knot B shows receding motions. Similarly, the apparent receding motion of the H $\alpha$  gas, which appears as a large arc shell shape, is detected at the western side of knot B (around knots A and T) while the gas is approaching around knot C. However, the stellar components at knots A and C show approaching motions while they are receding at knot B. The irregular stellar velocity is not a circular rotation disk within Haro 11 but a complex merging system. Menacho et al. (2019) studied the slices of the H $\alpha$  emission in velocity space and compared the ratio maps of  $[\text{O III}]\lambda 5007/\text{H}\alpha$  and  $[\text{O I}]\lambda 6300/\text{H}\alpha$ . The authors reported the existence of an expanding shell (arc shell shape at the western side of knot B) and the outflows of ionized gas around knot C. The CO(1–0) also shows the approaching (and receding) motions at knot C (and B), similar to that of H $\alpha$ , which may indicate the presence of molecular outflows. Furthermore, we note a clear stellar velocity edge between knots B and C, which probably indicates the collision of stellar components from the galaxy progenitor. Thus, the molecular gas between knots B and C might be the complex or combined stage of collision and feedback.

In Fig. 3, we present the CO(1–0) and H $\alpha$  spectra within knots B and C, the  $r \sim 0.6''$  region between B and C (hereafter B/C), and the total area. We performed one Gaussian function fitting for the CO(1–0) and H $\alpha$  spectra in each region. Adopting the systemic CO velocity as  $6051.3 \pm 2.1 \text{ km s}^{-1}$ , the CO velocity in knot B (C) is redshifted (blueshifted), which is consistent with the CO velocity map in Fig. 2. However, the H $\alpha$  velocity in knots B and C is blueshifted, which is different from the CO velocity. After subtracting the instrument resolution from the fitted Gaussian widths, we compute the velocity dispersion of H $\alpha$  and CO gas. We note that knot B shows the highest velocity dispersion value of CO and H $\alpha$  emission, indicating the strongest starburst activity in Haro 11. Furthermore, the velocity dispersion of CO and H $\alpha$  emission at knot C is also high, which we discuss below. To clearly understand the molecular gas distribution in Haro 11, we present the CO(1–0) channel maps at widths of  $20 \text{ km s}^{-1}$  in Fig. 4, contoured on the stellar image from MUSE data.

In Fig. 5, we present the intensity-weighted velocity dispersion (moment 2,  $\sigma_v$ ) maps of CO(1–0) (left panel) and H $\alpha$  (right panel) emission lines. We note that the CO(1–0) velocity dispersion within and between knots B and C, which contain the high surface density gas, is larger than the relatively diffuse gas in the outer regions. The highest velocity dispersion values of CO gas are detected in the lane extending from knots B toward the south-east. This shape is consistent with the  $[\text{N II}]\lambda 6583$  enriched area and then toward the high H $\alpha$  velocity dispersion region (see Fig. 3 in Menacho et al. 2021), indicating strong starburst activity; for example, Wolf–Rayet (WR) stars occur within the collision and overlap region of molecular gas. However, the large velocity dispersion might also be caused by the beam-smearing effect.

### 3.3. Spatial star formation efficiencies and specific star formation rate

To investigate the relative strength of star formation activities, we discuss the SFE and specific SFR. There are a few different

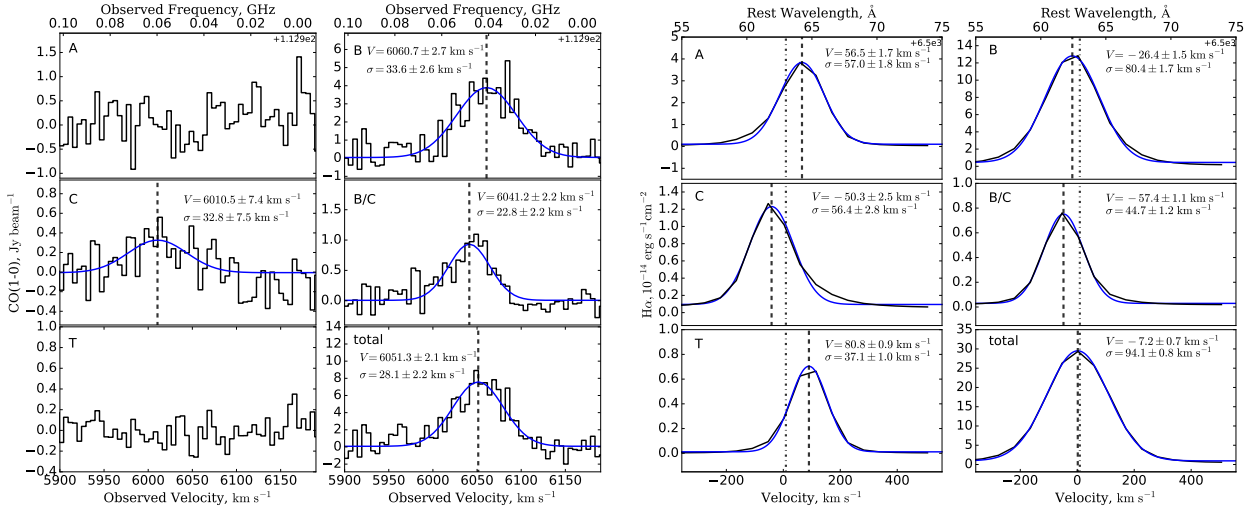


**Fig. 3.** Spectra of CO(1–0) and H $\alpha$  emission in Haro 11. *Left:* CO(1–0) spectra collected from the knots (A, B, C, T), the region ( $r \sim 0.6''$ , marked as B/C) between B and C, and the entire CO region. *Right:* H $\alpha$  spectra collected from the knots (A, B, C, T), the region between B and C marked B/C, and the  $R_{80}$  region. The dash-dotted lines show the rest-frame wavelength of the H $\alpha$  emission line. In each panel, blue lines represent the best one-Gaussian fitting spectra, attached with the relevant results, for example, the velocity of CO and systemic velocity subtracted velocity of H $\alpha$ . The velocity dispersion  $\sigma$  values are derived from the Gaussian widths by subtracting the instrument resolution. Dashed lines represent the fitting velocity of CO and H $\alpha$ .

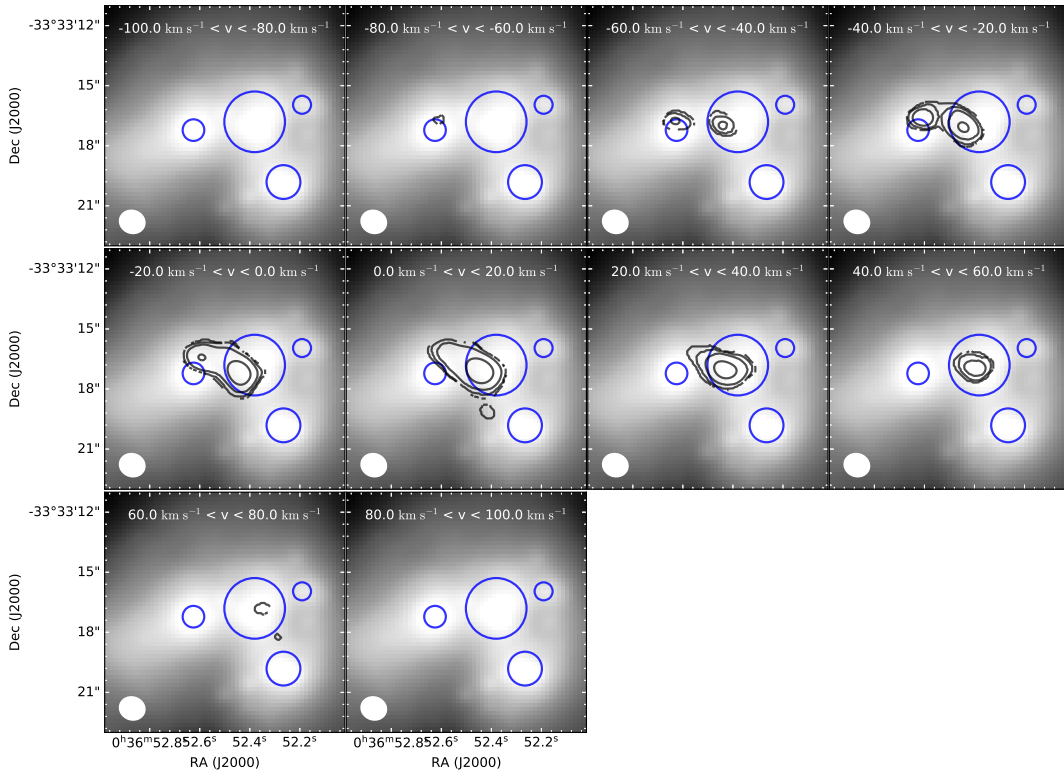


**Fig. 4.** CO(1–0) channel maps of Haro 11 contoured on the optical stellar continuum image. The spectral channel width of the original CO(1–0) cube is rebinned to 20 km s $^{-1}$ . The blue circles represent the four starburst knots, in an identical way to in Fig. 1. The black contours show the intensity map at levels of 3, 6, 12 (and so on) times the rms. The beam size of CO(1–0) is marked as the elliptical white circle in the bottom-left corner of each panel.

definitions for SFE (Leroy et al. 2008; Kennicutt & Evans 2012), but we take it to be the ratio of SFR and molecular H $_2$  gas mass (SFR/ $M_{H_2}$ , or  $\Sigma_{SFR}/\Sigma_{M_{H_2}}$ ) throughout this paper. The SFE is the inverse of the molecular gas depletion time, with units of yr $^{-1}$ , meaning the time required to consume the molecular gas at the present-day star formation. The specific SFR (sSFR), defined

as SFR/ $M_*$  or  $\Sigma_{SFR}/\Sigma_{M_*}$ , represents the stellar mass birthrate in galaxies, and can help to characterize the star formation history.

We adopted a Gaussian kernel and used the CASA task *imsmooth* to smooth the original SFR and  $M_*$  maps. We set the resolution of target maps as the beam size of the CO(1–0)

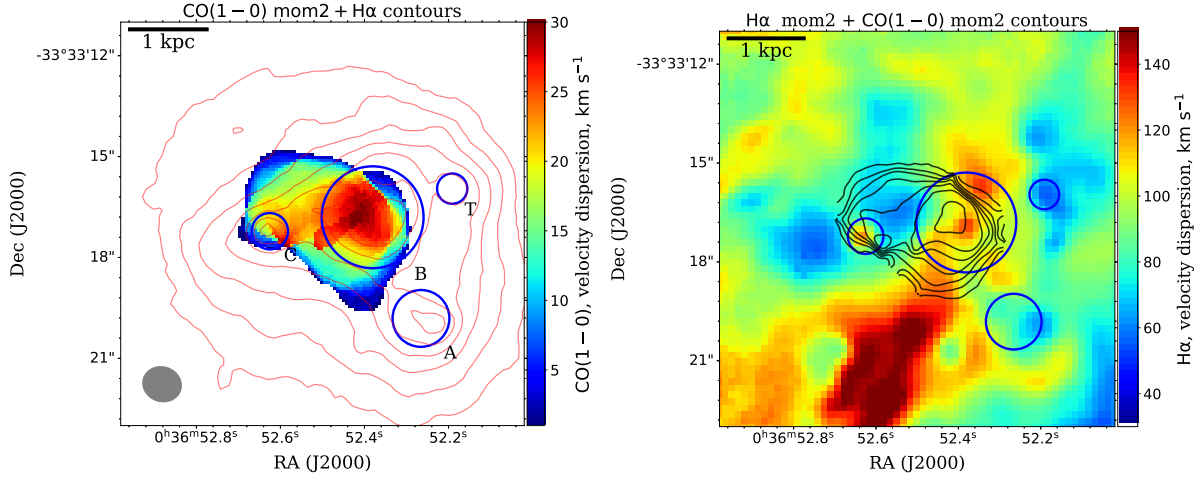


**Fig. 5.** Velocity dispersion of gas emission in Haro 11. *Left:* velocity dispersion (moment 2) of CO(1–0) emission line contoured by H $\alpha$  flux. *Right:* velocity dispersion of H $\alpha$  contoured by CO(1–0) velocity dispersion. Other symbols are the same as in Fig. 1.

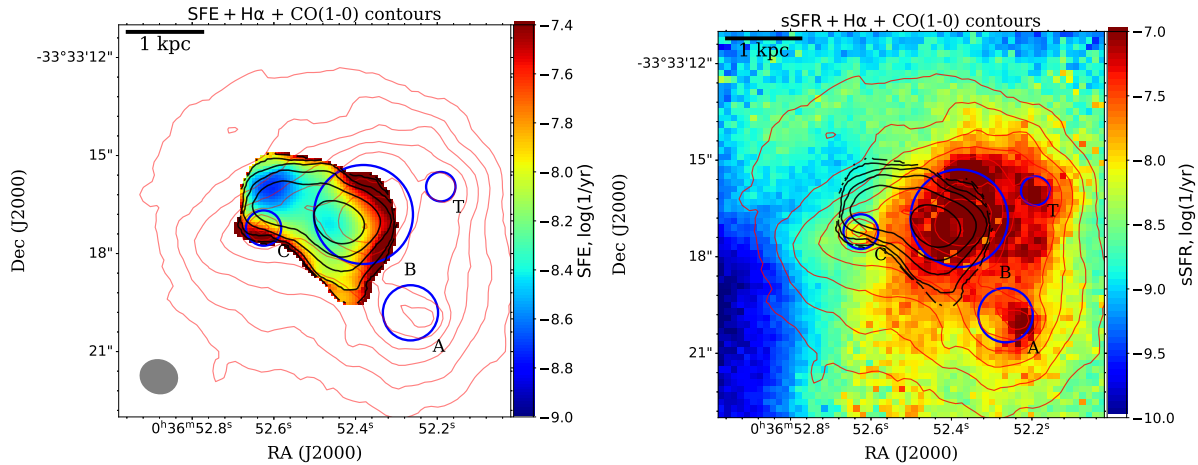


**Fig. 6.** Maps of SFE (*left panel*) and specific SFR (sSFR, *right panel*) contoured by H $\alpha$  (red) and CO(1–0) (black) fluxes. Other symbols are the same as in Fig. 1.

image, and then computed the spatial distribution of the SFE and specific SFR (sSFR). In Fig. 6, we show the SFE and sSFR distribution maps overlaid by H $\alpha$  and CO(1–0) fluxes. The logarithmic SFE values range from  $-9.0$  to  $-7.0$ , which are about 0.2–2.0 dex higher than the main sequence of normal star-forming galaxies in the local Universe (Kennicutt & Evans 2012). The highest SFE value is detected in the northwestern edge of knot B, which consists of the local peaks of H $\alpha$  emission, but molecular gas surface density is relatively low. The logarithmic sSFR values range from  $-9.0$  to  $-7.0$ , about 1.0–3.0 dex above the main sequence of normal star-forming galaxies in the local Universe (Saintonge et al. 2016). We find the highest sSFRs are detected in knot B, indicating that the stellar mass assembles efficiently therein. Furthermore, because of the presence of a large amount of molecular with weak H $\alpha$  emission in the northern and eastern regions, toward knots C and B, the sSFRs and SFEs are relatively small. However, the molecular gas will provide the fuel for future star formation around knot B.

### 3.4. Global star formation

In Sect. 3.3, we illustrate the spatial distribution of SFE and sSFR. In this section we compare the global SFE and SFR of Haro 11 with other galaxies in the literature and explore the

possible evolutionary path of such a late-stage merger system. We calculate the gas mass from CO(1–0) luminosity to be about  $3.8^{+3.3}_{-3.1} \times 10^9 M_{\odot}$ , for which the uncertainty is caused by the  $\alpha_{\text{CO}}$  range and the three times CO intensity rms. In Fig. 7, we present the Kennicutt–Schmidt (K–S) law and main sequence relation for Haro 11 and other galaxy samples. The data include individual GMCs in the nearby spiral galaxy M33 (Gratier et al. 2010), individual star-forming regions (and global properties) of the merger system NGC 4038/4039 (Gao et al. 2001; Lahén et al. 2018; Tsuge et al. 2021), spatially resolved measurements of 12 spiral galaxies (Bigiel et al. 2008; Shi et al. 2011), and nearby merger (U)LIRGs (Shangguan et al. 2019; Wilson et al. 2019). In addition, the data also include the global properties of post-starburst galaxies (Smircina et al. 2018, 2022), nearby merging dwarf systems (Paudel et al. 2018), high- $z$  main sequence galaxies ( $z \sim 1.2$ – $2.2$ , Tacconi et al. 2013), and starburst galaxies ( $1.2 < z < 6.3$ , see the references in Shi et al. 2018). We also overlay the  $M_{*}$ –SFR distribution of all of the galaxies derived from the SDSS DR8 MPA-JHU catalog<sup>4</sup>. The K–S law (Kennicutt et al. 2007) and main sequence relation (Saintonge et al. 2016) for local galaxies are shown as solid

<sup>4</sup> [https://www.sdss.org/dr12/spectro/galaxy\\_mpa\\_jhu/](https://www.sdss.org/dr12/spectro/galaxy_mpa_jhu/)



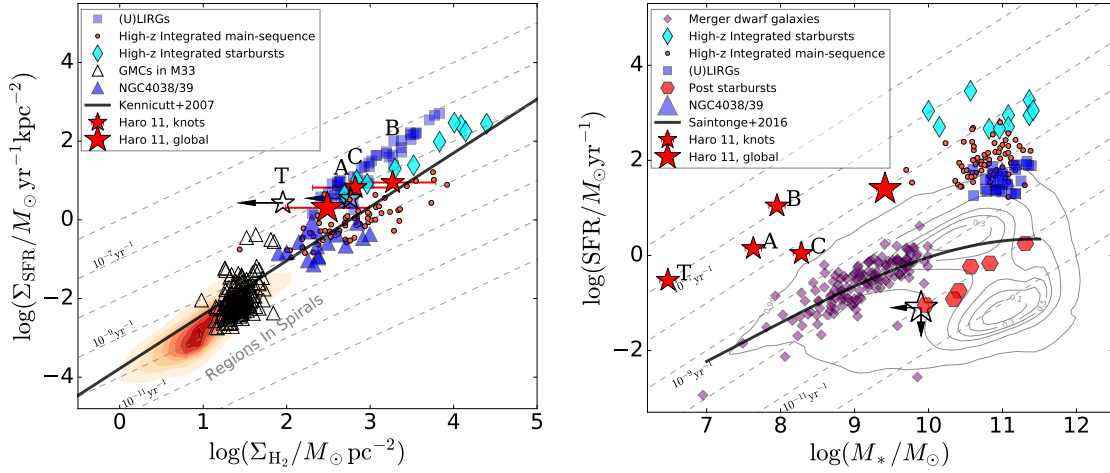


**Fig. 7.** Scaling relations of Haro 11 and other galaxies. *Left:* Kennicutt–Schmidt law, gas surface density  $\Sigma_{\text{H}_2}$  vs. SFR surface density  $\Sigma_{\text{SFR}}$ , for different galaxy samples. Red stars mark the knots in Haro 11, and a larger red star shows the global value. Because of the lack of CO detection at knots A and T, the upper limited  $\Sigma_{\text{H}_2}$  are shown as white stars. The star-forming clumps in the nearby merger Antennae (NGC 4038/4039) galaxy are marked as blue triangles (Tsuge et al. 2021), the global value is shown as the larger blue triangle (Gao et al. 2001; Lahén et al. 2018). The spatially resolved properties in nearby (U)LIRGs from Wilson et al. (2019) are marked as blue squares. Other samples are collected from Shi et al. (2018), including local spiral galaxies (red contours, Bigiel et al. 2008; Shi et al. 2011), giant molecular clouds in M33 (white triangles, Gratier et al. 2010), high- $z$  main sequence galaxies (red circles:  $z \sim 1.2\text{--}2.2$ , Tacconi et al. 2013), and starburst galaxies (cyan diamonds:  $1.2 < z < 6.3$ , see the references in Shi et al. 2018). The black line represents the K–S law derived by Kennicutt et al. (2007). The gray dashed lines represent different SFE levels. *Right:* main sequence relation, stellar mass  $M_*$  vs. SFR, for different galaxy samples. Global properties of massive merger (U)LIRGs from Shangguan et al. (2019) are shown as blue squares. Post starburst galaxies from Smercina et al. (2018, 2022) are represented with hexagons, in which the SFRs are estimated with the FUV fluxes from GALEX all-sky survey. The purple diamonds represent the merging dwarf galaxies in the local Universe (Paudel et al. 2018), in which the SFRs are estimated with the FUV fluxes from GALEX all-sky survey. Gray contours indicate all of the galaxies derived from the SDSS DR8 MPA-JHU catalog. The main sequence relation of SFGs in the local Universe is shown as a solid black line (Saintonge et al. 2016). The gray dashed lines represent different sSFR levels. The white star indicates the post-starburst phase of Haro 11 in the future, where arrows represent the upper limit values of stellar mass and SFR. Other symbols are the same as in the left panel.

black lines. The individual knots in Haro 11 are marked as red stars, while the global value is shown as a larger red star.

We find that star-forming regions in the disk of spiral galaxies (including M33) overlap regions of NGC 4038/4039, and high- $z$  normal SFGs follow the well-defined K–S law from Kennicutt et al. (2007). We find the star formation at knot B is nearly consistent with the K–S law. However, the global SFEs of Haro 11 and knot C are significantly higher ( $\sim 0.5$  dex) than these normal SFGs and NGC 4038/4039. The molecular gas depletion time in Haro 11 (and its knots) is similar to the high- $z$  starburst galaxies and star-forming regions in nearby (U)LIRGs. These nearby interacting dwarf galaxies ( $M_* < 10^{10} M_{\odot}$ ,  $z < 0.02$ , Paudel et al. 2018), selected by visual inspection from both SDSS and DESI Legacy imaging<sup>5</sup> surveys, are consistent with the star-forming main sequence relation (Saintonge et al. 2016). Most of these galaxies are located at the pre-merger or early-merger stage, suggesting that the significant enhancement of star formation has not yet been triggered. The sSFRs ( $\geq 10^{-8} \text{ yr}^{-1}$ ) of Haro 11 and its knots resemble those of high- $z$  starburst galaxies, which are about 0.6–2 dex higher than other galaxies. Adopting the  $H\alpha$ -based SFRs, Smercina et al. (2018, 2022) locate these post-starburst galaxies at the transition phase between major gas-rich mergers and gas-poor quiescent galaxies, where star formation is suppressed by continued injection of turbulent or mechanical heating.

Considering the similar SFEs and sSFRs as high- $z$  starburst galaxies, as well as the small stellar mass and low metallicity ( $1/3 Z_{\odot}$ ), we can regard Haro 11 as an analog of high- $z$  dwarf starburst galaxies. We explore the molecular and neutral gas depletion and discuss the evolution path in Sect. 4.4.

### 3.5. [C I] distribution

Though the CO emission line is commonly used as the molecular gas tracer in the ISM, its reliability is dependent on the optical depth, metallicity, and radiation strength. Previous observations (Ikeda et al. 2002; Shimajiri et al. 2013) find that neutral carbon is well mixed throughout the clouds, and is not only located at the layer interface between the ionized carbon regions and the shielded CO molecule cores. Furthermore, the integrated intensity ratios ( $R = I_{[\text{C I}]} / I_{\text{CO}(1-0)}$ ) are significantly higher in active nuclear environments than in galactic clouds. Cosmic rays from supernovae, ultraviolet (UV) radiation from starburst, and the mechanical shocks dissociate CO molecules, significantly enhancing carbon abundance (Tanaka et al. 2011; Krips et al. 2016; Bisbas et al. 2017; Papadopoulos et al. 2018). These findings suggest that neutral carbon can be a complementary molecular gas tracer to CO, especially in active galaxies.

Here we present our analysis of the spatially resolved [C I] line emission with ALMA band 8 observations and the line ratios of [C I] to CO in Haro 11, and then our evaluation of its potential as a complementary  $\text{H}_2$  tracer. We smooth the CO and [C I] brightness images to a larger beam size of  $1.5'' \times 1.5''$  ( $\sim 630 \times 630$  pc), with the same pixel size of  $0.1''$ . In Fig. 8, we provide the spatial distribution of the CO(1–0) and [C I] emission intensity and velocity, as well as their line intensity ratios. We note the [C I](1–0) line emission is detected throughout the bridge from knot B to C, in which the peak location and distribution strongly resemble the CO line emission. We also check the velocity distribution of [C I](1–0), which presents a similar trend to the velocity of CO(1–0) shown in Fig. 2. These results seem to suggest that [C I] can trace the same molecular gas as

<sup>5</sup> <https://www.legacysurvey.org/>

CO in such a dwarf merger starburst galaxy. Previous studies (Israel et al. 2015; Jiao et al. 2019) reported that [C I] luminosity is associated with the CO(1–0) or CO(2–1) emission, suggesting that the [C I] can trace the molecular gas in H II, Seyfert, and starburst galaxies at kiloparsec scales. Using the [C I] to H<sub>2</sub> conversion calibration of (Eq. (1) and Fig. 6, Madden et al. 2020), we estimate the H<sub>2</sub> gas mass to be  $\sim 5.3 \times 10^8 M_{\odot}$  and  $\sim 2.1 \times 10^8 M_{\odot}$  (see Table 2) at the metallicities of 0.1  $Z_{\odot}$  and 0.25  $Z_{\odot}$ , respectively. The calculation uncertainty is about 0.3 dex. The [C I]-based H<sub>2</sub> gas mass is much smaller than the median value of CO-based H<sub>2</sub> gas mass, but is nearly consistent with the gas mass range considering the calibration uncertainty. This difference may be due to the larger  $\alpha_{\text{CO}}$  that we adopted or the amount of missing flux in the [C I] observation. Further studies are needed to identify possible limitations for [C I] tracing H<sub>2</sub> and how [C I] emission translates to H<sub>2</sub> mass. Furthermore, in the bottom-right panel of Fig. 8, we compare the [C I]/CO(1–0) ratios in Haro 11 with the disks of spiral galaxies ( $R \sim 0.11$ , Jiao et al. 2019), (U)LIRGs ( $R \sim 0.23$ , Jiao et al. 2017, 2019), and the nuclear outflow region of the nearby starburst galaxy NGC 253 ( $R \sim 0.4\text{--}0.6$ , Krips et al. 2016). We rebinned the pixels in [C I] and CO(1–0) intensity maps as  $0.4''$ . Though the pixel size is smaller than the beam sizes of CO and [C I], it is instructive to perform such a comparison. We note the line ratios of [C I]/CO range from 0.35 to 0.55 within the two local peak molecular gas components, which are significantly enhanced concerning the values of normal spiral galaxies and (U)LIRGs while being similar to the outflow region of NGC 253. Krips et al. (2016) supposed the high ratios in NGC 253 indicate that shocks, associated radiation, and/or cosmic rays affect the carbon and CO excitation and their abundance. Meanwhile, the line ratios in the northern region of knot C are higher than 0.45, and are systematically higher than in the central region of knot B. To explain this [C I] enrichment, we need to remember that Haro 11 is one of the most extreme starburst galaxies in the nearby Universe. Hayes et al. (2007) detected strong Ly $\alpha$  emission extending from knot C to its north and south sides, probably indicating a possible outflow. Recently, using the spectroscopy data from the HST/COS telescope/instrument, Östlin et al. (2021) found knot C has the lowest covering fraction ( $\leq 50\%$ ) of neutral gas and the highest Ly $\alpha$  escape fraction. Their results suggested that knot C is the original region of the escaping Lyman continuum photons. The intense radiation, such as that in the form of cosmic rays and far-ultraviolet (FUV) photons, dissociates the CO molecules and enhances the neutral carbon abundance. The higher [C I]/CO(1–0) ratios may indicate the significant amount of molecular gas not traced by the CO emission, that is, CO-dark gas, contributing to the larger CO-to-H<sub>2</sub> conversion factor in such a metal-poor starburst galaxy (Bolatto et al. 2013).

## 4. Discussion

### 4.1. Molecular gas in knots A and T

The exciting finding is the relatively high sSFRs within knots A and T, with no significant CO detections, which is possibly because of the limited detection sensitivity of ALMA. Considering the high SFR values, the average SFEs within regions A and T might be more prominent than in knots B and C (left panel of Fig. 6). Analyzing the He II $\lambda$ 4686 features, James et al. (2013) reported that knot A contains about 900 young ( $\leq 5$  Myr) WR stars and presents typical nitrogen abundance. These authors suggested that the WR phase in knot A is ongoing while the ejected nitrogen-rich material does not have enough time to

**Table 2.** Properties of Haro 11.

Property	Unit	Value	Reference
Other name	...	ESO 350-IG38	1
RA (J2000)	h:m:s	00:36:52.7	1
Dec (J2000)	d:m:s	−33:33:17	1
$V_{\text{sys}}$ (optical)	km s <sup>−1</sup>	6194 ± 5.1	2
Redshift	...	0.0206467	2
Distance	Mpc	87.2 ± 6.1	3
Scale	pc/arcsec <sup>−1</sup>	~420	3
$M_*$	10 <sup>9</sup> $M_{\odot}$	2.6 ± 0.8	4
$V_{\text{sys}}$ (CO)	km s <sup>−1</sup>	6051.3 ± 2.1	4
CO(1–0) flux	Jy km s <sup>−1</sup>	3.3 ± 0.1	4
[C I] flux	Jy km s <sup>−1</sup>	7.4 ± 0.3	4
$M_{\text{H}_2}$ (CO)	10 <sup>9</sup> $M_{\odot}$	3.8 <sup>+3.3</sup> <sub>−3.1</sub>	4
$M_{\text{H}_2}$ ([C I])	10 <sup>8</sup> $M_{\odot}$	2.1–5.3	4
$M_{\text{HI}}$	10 <sup>8</sup> $M_{\odot}$	5.1	5
SFR <sub>Ha+TIR</sub>	$M_{\odot}$ yr <sup>−1</sup>	25.1 <sup>+28.6</sup> <sub>−13.4</sub>	6
SFR <sub>Ha(HST)</sub>	$M_{\odot}$ yr <sup>−1</sup>	24.0	7
SFR <sub>TIR</sub>	$M_{\odot}$ yr <sup>−1</sup>	28.6	8
SFR <sub>Ha</sub>	$M_{\odot}$ yr <sup>−1</sup>	25.1 ± 0.4	4
Size	kpc <sup>2</sup>	12.5	4
$\sigma_v$	km s <sup>−1</sup>	17.2 <sup>+8.3</sup> <sub>−11.5</sub>	4
$P_{\text{turb}}$	10 <sup>6</sup> K cm <sup>−3</sup>	3.4 <sup>+10.2</sup> <sub>−3.2</sub>	4
$\alpha_{\text{vir}}$	...	0.17 <sup>+0.11</sup> <sub>−0.06</sub>	4

**Notes.** The Kroupa (2001) IMF is used to derive the stellar mass and SFR in this work. We assume the CO-H<sub>2</sub> conversion factor  $\alpha_{\text{CO}}$  as 60  $M_{\odot}$  (K km s<sup>−1</sup> pc<sup>−2</sup>)<sup>−1</sup>, with a range of 10–110  $M_{\odot}$  (K km s<sup>−1</sup> pc<sup>−2</sup>)<sup>−1</sup>. We used the Python packages *Starmorph* to estimate the radius  $R_{80}$  containing 80% flux in  $r$  band, and then calculated the size of Haro 11. The CO(1–0) velocity dispersion  $\sigma_v$ , internal turbulent pressure  $P_{\text{turb}}$  and the virial parameter  $\alpha_{\text{vir}}$  are shown as the median values with one-sigma ranges. We also used the [C I] luminosity to derive the molecular gas based on the calibration in Madden et al. (2020) at metallicities of 0.25  $Z_{\odot}$  and 0.1  $Z_{\odot}$ , respectively, with a systemic uncertainty of 0.3 dex. **References.** (1) Östlin et al. (2015); (2) Menacho et al. (2021); (3) NED; (4) this work; (5) Pardy et al. (2016); (6) Rémy-Ruyer et al. (2015); (7) Hayes et al. (2007); (8) Madden et al. (2013).

cool down and mix with the warm ISM. Knot T is located toward one of the lobes of the dusty arm extending from A to T (Menacho et al. 2019, 2021). Menacho et al. (2019) found the dusty arm shows an arc resembling an expanding ionized gas shell with a velocity of about 50 km s<sup>−1</sup>. The compression of molecular gas might trigger the star formation within knot T. The molecular gas within knots A and T has been partly consumed by the intense star-formation or destroyed by the strong existing radiation and shocks. Much deeper observations with the ALMA telescope are needed to investigate the accurate mass distribution and kinematics of molecular gas.

### 4.2. Molecular gas properties in previous studies

To investigate gas and dust properties in low-metallicity environments, Madden et al. (2013) performed an extensive program, named the Dwarf Galaxy Survey (DGS). This program observed about 50 metal-poor dwarf galaxies at the far-infrared (FIR) and sub-millimeter bands with the *Herschel* Space Observatory. The metallicities of these nearby DGS galaxies range from  $\sim 2.5\%$   $Z_{\odot}$  (I Zw 18) to  $\sim 1$   $Z_{\odot}$  (He 2–10). Haro 11 is also included in

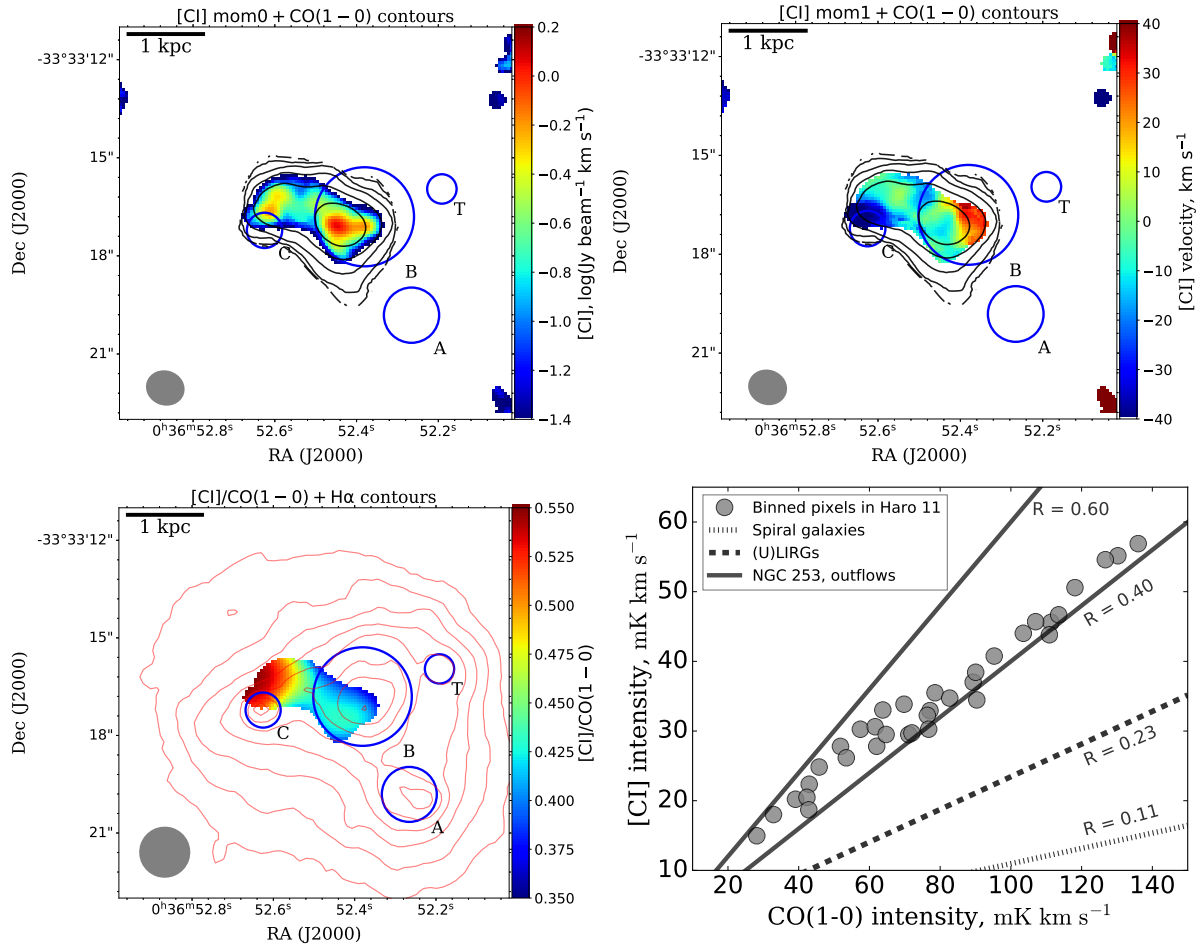


**Fig. 8.** [C I] emission distribution in Haro 11. *Upper:* distribution of [C I](1–0) emission (color) intensity (*left*) and velocity (*right*) contoured with the CO(1–0) emission (black contours), with levels of  $(1/2)^n$  ( $n = 1, 2, \dots, 8$ ) times of the maximum value of CO intensities. *Bottom-left:* distribution of the line ratio ( $R = I_{\text{[C I]}}/I_{\text{CO(1-0)}}$ ) of the [C I] and CO emission intensity. Other symbols are the same as in Fig. 1. *Bottom-right:* integrated intensity of [C I] pixels versus CO(1–0), in units of  $\text{mK km s}^{-1}$ . The pixels in Haro 11 are rebinned as  $\sim 0.4''$ . The average ratios in the disks of spiral galaxies and in (U)LIRGs reported by Jiao et al. (2019) are shown as dotted ( $R \sim 0.11$ ) and dashed ( $R \sim 0.23$ ) lines, respectively. Black solid lines represent the ratios ( $R \sim 0.4\text{--}0.6$ ) in the outflow regions that emerge from the nucleus of NGC 253 (Krips et al. 2016).

the DGS, showing the highest global SFR (Madden et al. 2013; Cormier et al. 2019).

The molecular gas tracer CO(1–0) in Haro 11 was not detected by the Mopra telescope (Cormier et al. 2014). However, two other tracers, the CO(2–1) and CO(3–2) lines, are observed with the Atacama Pathfinder EXperiment (APEX). The beam sizes for CO(2–1) and CO(3–2) observations are about  $26''$  and  $17''$ , respectively, which are much larger than the ALMA observation in this work. To convert the CO(2–1) and CO(3–2) intensities to CO(1–0) intensity, Cormier et al. (2014) adopted the CO(2–1)/CO(1–0) ratio ( $R_{21}$ ) as 0.8 and CO(3–2)/CO(1–0) ratio ( $R_{31}$ ) as 0.6 (Leroy et al. 2008; Wilson et al. 2009). To estimate the  $\text{H}_2$  gas mass, Cormier et al. (2014) adopted two different CO-to- $\text{H}_2$  conversion factors, one is the Galactic value ( $X_{\text{CO}} = 2.0 \times 10^{20} \text{ cm}^{-2} (\text{K km s}^{-1})^{-1}$ , or  $\alpha_{\text{CO}} = 4.3 M_{\odot} (\text{K km s}^{-1} \text{ pc}^{-2})^{-1}$  Bolatto et al. 2013), while the other is ten times that of the Galactic value. Based on these two conversion factors, the  $\text{H}_2$  gas mass in Haro 11 is estimated as  $2.5 \times 10^8 M_{\odot}$  and  $2.5 \times 10^9 M_{\odot}$ , respectively. The former value is smaller than our  $\text{H}_2$  gas mass estimation ( $3.8^{+3.3}_{-3.1} \times 10^9 M_{\odot}$ ) in this work, because the conversion factor of (one times) the Galactic value would underestimate the molecular gas mass in low-metallicity galaxies (Shi et al. 2016; Madden et al. 2020).

Meanwhile, the latter ( $2.5 \times 10^9 M_{\odot}$ ) is consistent with our estimation. Furthermore, Cormier et al. (2014) also provide the total molecular gas mass derived from the dust measurements from *Herschel* observations (Rémy-Ruyer et al. 2013, 2015). Rémy-Ruyer et al. (2015) performed a full dust SED modeling for photometric measurements up to  $500 \mu\text{m}$ , and calculated the dust mass in Haro 11 to be about  $9.9 \times 10^6 M_{\odot}$ . Adopting the dust-to-gas ratio (D/G) as 1/150 at a metallicity of 8.7, Cormier et al. (2014) estimated the  $\text{H}_2$  gas mass as  $3.6 \times 10^9 M_{\odot}$ . Our result ( $3.8^{+3.3}_{-3.1} \times 10^9 M_{\odot}$ ) is consistent with the dust-based  $\text{H}_2$  estimation of Cormier et al. (2014), which suggests that the assumption of  $\alpha_{\text{CO}}$  in this work is appropriate considering the probable CO-dark molecular gas in low-metallicity galaxies (Madden et al. 1997, 2020; Madden 2000; Wolfire et al. 2010).

Cormier et al. (2014) found the SFR surface density of Haro 11 is about 2 dex above the K–S relationship, given the low-gas-mass surface density using CO to trace the total  $\text{H}_2$  gas mass. However, in Fig. 7, our ALMA observations put Haro 11 closer to the K–S relationship, that is, less than 0.5 dex above, which is consistent with the findings of Madden et al. (2020) that star-forming galaxies fall close to or on the K–S law when taking the CO-dark gas into account. Given the similar  $\text{H}_2$  gas mass estimations, the difference in the position in the gas mass



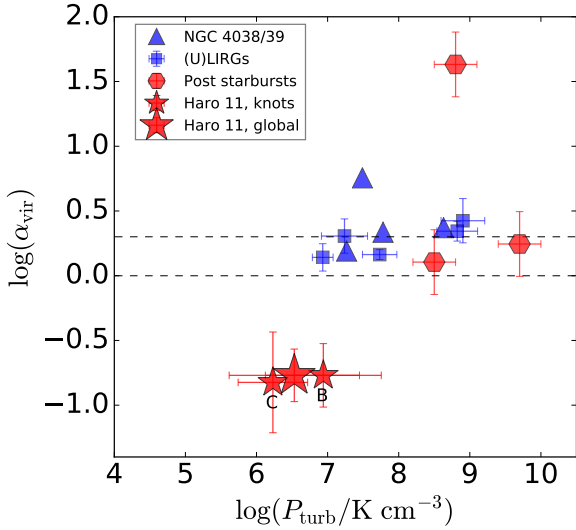


**Fig. 9.** Comparison of the turbulent pressure ( $P_{\text{turb}}$ ) and the virial parameter ( $\alpha_{\text{vir}}$ ) between Haro 11 and other types of galaxies. The properties of knots B, C, and Haro 11 are shown as red stars. Blue squares represent the global properties of five (U)LIRGs calculated from the pixel-binned measurements of [Wilson et al. \(2019\)](#). The global properties of three post-starburst galaxies derived by [Smercina et al. \(2022\)](#) are shown as red hexagons. Blue triangles represent the four massive, young cluster-forming regions located at the overlap region of NGC 4038/4039 ([Tsuge et al. 2021](#)). The error bars cover the 16–84% widths of the distribution of  $P_{\text{turb}}$  and  $\alpha_{\text{vir}}$  across all resolved regions in each galaxy. Dashed lines represent the levels of  $\alpha_{\text{vir}} = 1, 2$ , respectively.

surface density – SFR surface density diagram is caused by the different estimations of galaxy size. [Cormier et al. \(2014\)](#) used the area size about  $1266 \text{ kpc}^2$  derived from the *Herschel* photometry apertures ([Rémy-Ruyer et al. 2013](#)), while we adopt the area size of about  $13 \text{ kpc}^2$  calculated from the radius  $R_{80}$  in  $r$  band image. The different aperture sizes cause this difference. The circular aperture size of Haro 11 in the FIR band is about  $45''$  ([Rémy-Ruyer et al. 2013](#)), which determines the morphology properties traced by the dust emission. However, using the high-spatial-resolution image from MUSE, we find the  $R_{80}$  is about  $5''$ , which covers all of the observed CO emission by ALMA and more than 95% of the  $\text{H}\alpha$  emission from MUSE. The area size of Haro 11 in our work focuses on the area around the brightest star-forming regions. Using different area sizes, Haro 11 shows an offset in the gas mass surface density–SFR surface density diagram. However, the total gas depletion time in this work is still consistent with that found by [Cormier et al. \(2014\)](#).

#### 4.3. Turbulent pressure and virial parameter

Though showing similar morphology and kinematics to the merger galaxy NGC 4038/4039 ([Östlin et al. 2015](#)), we note the SFE and sSFR values of star-forming regions in Haro 11 are much larger than those in NGC 4038/4039 and some (U)LIRGs. The gas surface densities of knots B (C) are about  $1860$  ( $660$ )  $M_{\odot} \text{ pc}^{-2}$ , which are systemically larger than the overlap and spiral regions in NGC 4038/4039, supporting the probable explanation that molecular gas is much denser in Haro 11 ([Östlin et al. 2015](#)). Furthermore, we estimated the turbulent pressure ( $P_{\text{turb}}$ ) and virial parameter ( $\alpha_{\text{vir}}$ ) in order to investigate why there are different SFEs within star-forming regions in these galaxies.

The virial parameter in a molecular cloud describes the balance between its kinetic energy and gravitational potential ([Krumholz & McKee 2005](#); [Kauffmann et al. 2013](#); [Sun et al. 2018](#)). Molecular cloud fragments are supercritical, unstable, and tend to collapse when  $\alpha_{\text{vir}} < 2$ , while the gas motion therein may prevent fragments from collapsing if  $\alpha_{\text{vir}} > 2$ . The virial parameter is important in determining the possibility of whether or not the clouds can form stars (clusters). However, in addition to self-gravity, the magnetic field and external gravitational potential also regulate the cloud dynamics in some environments, such as galaxy outer regions with low gas densities and the galactic center with high ambient pressure ([Heyer et al. 2001](#); [Oka et al. 2001](#); [Sun et al. 2018](#); [Smercina et al. 2022](#)). When assuming pressure equilibrium within a gas cloud, the internal turbulent pressure (internal kinetic energy density) will be equal to the external pressure, which has been emphasized in previous studies of galactic clouds ([Field et al. 2011](#); [Barnes et al. 2020](#); [Krieger et al. 2020](#)). Giant molecular clouds in the Milky Way have typical radii ranging from 5 to 200 pc ([Murray 2011](#)). The radius of the synthesized beam in our CO(1–0) observation of Haro 11 is about 220 pc, slightly larger than the range of Galactic molecular cloud sizes. We assume that the beam size represents the relevant cloud size scale in the following analysis of the virial parameter and turbulent pressure.

Following [Sun et al. \(2018\)](#), we estimate the  $P_{\text{turb}}$  and  $\alpha_{\text{vir}}$  at the scale of the beam size through the following equations:

$$\alpha_{\text{vir}} \approx \frac{5\sigma^2 r_{\text{beam}}}{fGM} = \frac{5 \ln 2}{\pi f G} \left( \frac{\sigma_v}{\text{km s}^{-1}} \right)^2 \left( \frac{\Sigma_{\text{tot}}}{M_{\odot} \text{ pc}^{-2}} \right)^{-1} \left( \frac{r_{\text{beam}}}{\text{pc}} \right)^{-1}, \quad (4)$$

$$P_{\text{turb}}/k_B \approx 61.3 \text{ K cm}^{-3} \left( \frac{\Sigma_{\text{H}_2}}{M_{\odot} \text{ pc}^{-2}} \right) \left( \frac{\sigma_v}{\text{km s}^{-1}} \right)^2 \left( \frac{r_{\text{beam}}}{40 \text{ pc}} \right)^{-1}. \quad (5)$$

In these equations, the factor  $f$  is about  $10/9$  based on a density profile  $\rho(r) \propto r^{-1}$  ([Sun et al. 2018](#)). The gravitational constant  $G \approx 4.3 \times 10^{-3} \text{ pc } M_{\odot}^{-1} (\text{km s}^{-1})^2$ , and  $r_{\text{beam}}$  is the radius of the synthesized beam. The  $\Sigma_{\text{tot}}$  is the surface density of total mass, including the stellar mass and gas mass. In Fig. 9, we perform a comparison of the turbulent pressure and the virial parameter between Haro 11, (U)LIRGs, NGC 4038/4039, and post-starburst galaxies. The values of  $\alpha_{\text{vir}} = 1, 2$  are marked as dashed lines. We note that the  $\alpha_{\text{vir}}$  and  $P_{\text{turb}}$  of knots B and C are significantly smaller than those of the clumps in massive merger system NGC 4038/4039, which probably lead to the higher SFE values in the starburst regions of Haro 11. Meanwhile, the median values of  $\alpha_{\text{vir}}$  and  $P_{\text{turb}}$  of Haro 11 are one to four orders of magnitude lower than the median values measured for star-forming regions of (U)LIRGs ([Wilson et al. 2019](#)) and post-starburst galaxies ([Smercina et al. 2022](#)). (U)LIRGs and post-starburst galaxies show larger  $\alpha_{\text{vir}}$  and  $P_{\text{turb}}$  values, supporting the negative feedback scenario, such that energy injection from AGNs and stellar feedback will dissipate and heat the molecular gas, suppress the star formation, and accelerate the quenching of star formation in the host galaxy. [James et al. \(2013\)](#) studied the  $\text{He II } \lambda 4686$  features and revealed large young WR populations ( $>1000$  stars) in knots A and B. In addition, bright X-ray emission is detected at and around knots B and C ([Grimes et al. 2007](#); [Gross et al. 2021](#)), possibly originating from two intermediate-mass black holes (IMBHs) with masses of about  $M_{\bullet} \gtrsim 7600 M_{\odot}$  and  $M_{\bullet} \gtrsim 20 M_{\odot}$ , respectively. Due to the complex kinematics of gas and stars in the center of the merger system, the IMBH therein might accrete the material rapidly and evolve into a supermassive black hole. The mechanical feedback from a massive black hole or the starburst, in the form of jets and outflows for example, will photoionize the



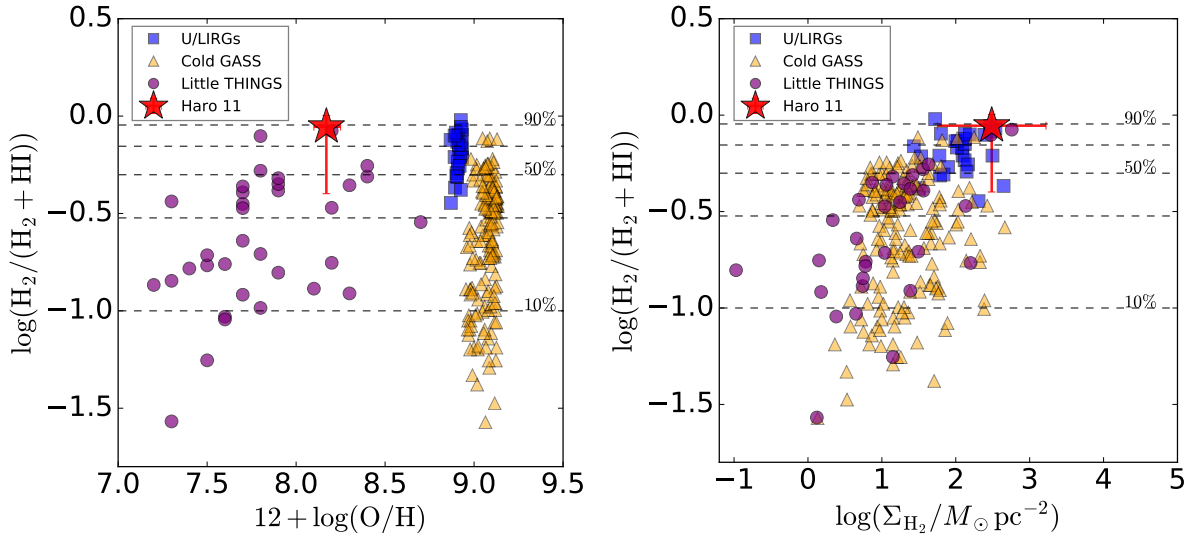


**Fig. 10.** Molecular gas fraction ( $M_{\text{H}_2}/(M_{\text{H}_2} + M_{\text{HI}})$ ) as a function of the average gas phase metallicity (*left panel*) and the average molecular gas surface density (*right panel*) in Haro 11 (red star) and other nearby galaxies. The (U)LIRGS sample is marked as blue squares, which is collected from the GOALS survey (Armus et al. 2009; Stierwalt et al. 2013; Shangguan et al. 2019) and cross-matched with the ALFALFA HI survey (Haynes et al. 2018), similar to the data in the right panel of Fig. 7. Black triangles represent normal star forming galaxies with  $M_* \geq 10^{10} M_\odot$  from the Cold GASS survey (Catinella et al. 2010, 2012, 2013). The nearby dwarf irregular or compact galaxies collected from the Little THINGS survey (Hunter et al. 2012, 2019) are shown as purple circles.

molecular gas and keep the ISM warm or cause them to escape from the host galaxy, thus suppressing star formation. Considering stellar feedback or the potential AGN activities in Haro 11, the turbulent pressure and the virial parameter probably follow a similar evolution trend to (U)LIRGs or post-starbursts, leading to a quenching timescale shorter than the molecular gas depletion time ( $1/\text{SFE}$ ,  $<0.15$  Gyr).

#### 4.4. Neutral gas

As the fuel of the molecular gas, neutral hydrogen gas is a prominent component of star-forming galaxies. To predict the evolution path of a merger system such as Haro 11, we need to consider the HI–H<sub>2</sub> transition and the fraction of HI gas. The spatial distribution and the kinematics of the HI gas are also essential to unravel the complex behaviors of molecular gas and star formation activities in Haro 11. However, based on the 24 h of observation with the VLA telescope (program 17B-287), Taft et al. (2019) did not detect HI emission, confirming the surprising lack of a neutral gas component within such a starburst galaxy (Pardy et al. 2016). The transition from HI to H<sub>2</sub> is affected by the gas density, dust, metallicity, and radiation in the interstellar medium (Sternberg et al. 2021). This section presents our comparison of the fraction of HI and H<sub>2</sub> in Haro 11 with normal SFGs, massive (U)LIRGs, and other dwarf galaxies, and our investigation of the possible reasons for these differences.

In Fig. 10, we show the molecular gas fraction ( $M_{\text{H}_2}/(M_{\text{H}_2} + M_{\text{HI}})$ ) as a function of the average gas-phase metallicity and the average molecular gas surface density in Haro 11 and other nearby galaxies. These nearby galaxies include the normal SFGs at  $M_* \geq 10^{10} M_\odot$  in the Cold GASS survey (Catinella et al. 2010, 2012, 2013), massive merger (U)LIRGs in the GOALS survey (Armus et al. 2009; Stierwalt et al. 2013; Shangguan et al. 2019) with the HI detection from the ALFALFA survey (Haynes et al. 2018), and the dwarf irregular and compact galaxies from the Little THINGS survey (Hunter et al. 2012, 2019). The molecular gas in the Cold GASS survey is determined from the CO(1–0) measurements from the IRAM 30-m telescope

(Catinella et al. 2010). Shangguan et al. (2019) performed the photometric spectral energy distribution fitting for (U)LIRGs in order to derive the total dust masses, and then adopted the gas-to-dust ratios to estimate the gas masses. Their gas mass estimations are consistent with the molecular gas derived from CO measurements for a subsample of GOALS objects (Larson et al. 2016; Shangguan et al. 2019). The molecular content of dwarf galaxies from the Little THINGS survey is calculated from the product of the total SFR and the typical molecular consumption time ( $\sim 2$  Gyr, Bigiel et al. 2008), using the method in Hunter et al. (2019). Meanwhile, we note that the gas consumption time of dwarf galaxies has a large uncertainty, ranging from  $\sim 50$  Myr to  $\sim 10$  Gyr (Hunt et al. 2015). Using the consumption times of 50 Myr and 10 Gyr, the H<sub>2</sub> gas fraction of Little THINGS galaxies is less than 10% and ranges from 10% to 90%, respectively. However, the large uncertainty on the H<sub>2</sub> gas fraction cannot change the trend that the gas fraction is dependent on the gas surface density, which we discuss below.

The metallicities of (U)LIRGs and normal SFGs are estimated from the stellar mass–metallicity relation (MZR) of Tremonti et al. (2004), and are systemically  $\sim 0.2$  dex below the MZR in the merger (U)LIRGs (Herrera-Camus et al. 2018). Meanwhile, to compute the average molecular gas surface densities of these galaxies, we used the Python packages *Statmorph*<sup>6</sup> (Rodríguez-Gomez et al. 2019) and *Photutils*<sup>7</sup> to calculate the radius ( $R_{80}$ ) containing 80% flux in *V* and *r* band images. Within these subsolar-metallicity dwarf galaxies, we note the molecular gas fraction ( $\sim 80\%$ ) of Haro 11 is rare, significantly larger than in normal SFGs, while being similar to that of the fraction ( $\sim 50\text{--}90\%$ ) of (U)LIRGs. At the similar metallicity, the molecular gas fraction in normal SFGs covers a large range ( $\sim 5\text{--}70\%$ ), probably indicating that the average metallicity is not the major property to affect the molecular gas fraction and the

<sup>6</sup> <https://statmorph.readthedocs.io/en/latest/overview.html>

<sup>7</sup> <https://photutils.readthedocs.io/en/latest/index.html>

HI–H<sub>2</sub> transition in the ISM. However, if compared with the average H<sub>2</sub> surface densities, the H<sub>2</sub> fraction is larger with higher gas densities among different types of galaxies. This result also supports the hypothesis that the HI–H<sub>2</sub> transition will be accelerated by the gravitational collapse in dense and optically thick regions (Sternberg et al. 2014, 2021). Though the average gas surface density of Haro 11 is about 300 M<sub>⊙</sub> pc<sup>-2</sup>, slightly higher than (U)LIRGs, the molecular gas is concentrated toward knots B and C, harboring high-surface-density molecular gas with Σ<sub>H<sub>2</sub></sub> > 660 M<sub>⊙</sub> pc<sup>-2</sup>.

Taking into account the deficient HI gas, intense starburst activities (higher SFE), and the potential stellar/AGN feedback, we estimated the upper limit values of gas depletion time and the final stellar mass of Haro 11 at the evolutionary end-stage. The gas depletion time ( $M_{\text{H}_2} + M_{\text{HI}}/$ SFR) will be shorter than 0.17<sup>+0.13</sup><sub>-0.12</sub> Gyr. Assuming that all of the molecular and neutral gas will form stars, the final stellar mass  $M_* + 1.36(M_{\text{H}_2} + M_{\text{HI}})$  will be smaller than 8.5<sup>+5.2</sup><sub>-5.0</sub> × 10<sup>9</sup> M<sub>⊙</sub>, including the factor 1.36 to account for the helium. Östlin et al. (2015) reported that Haro 11 shares a similar morphology and kinematics of stars and ionized gas with the Antennae galaxy. After performing a high-resolution smoothed particle hydrodynamic simulation, Lahén et al. (2018) reproduced both the observed morphology and the off-nuclear starburst of the Antennae galaxy. Lahén et al. (2018) also found that the Antennae galaxy will evolve into a red quiescent galaxy after 2.5 Gyr of secular evolution in their simulation. Given the lower stellar mass and the shallow gravitational potential of Haro 11, the ionized and molecular gas will escape the host galaxy efficiently, which will reduce the molecular gas depletion time. We predict that Haro 11 could be the potential progenitor of these nearby less massive elliptical galaxies. In the right panel of Fig. 7, we also point out the position of Haro 11 (marked as a white star) at the transition phase between SFGs and quiescent galaxies, where the stellar mass and SFR are assumed as their upper limit values. The sSFR at the transition phase is adopted as 10<sup>-11</sup> yr<sup>-1</sup> (Renzini & Peng 2015), which is similar to these post-starburst galaxies from Smercina et al. (2022) and green valley galaxies. In the future, we will perform a hydrodynamic particle simulation to reproduce the observed metallicity, star formation, gas fraction, and kinematics of gas and stars in Haro 11, aiming to investigate the merger remnants at different evolutionary stages.

## 5. Summary

In this work, using the archival ALMA (band 3, 8) and VLT/MUSE data, we study the spatially resolved molecular gas and neutral carbon gas in the dwarf merger starburst galaxy Haro 11. We explore the star formation and the gas consumption activities in different regions. Our main conclusions are summarized below.

- Molecular gas is assembled around the central star-forming regions (knots B and C), while no significant detection of CO(1–0) is found within knots A and T. The molecular and ionized gas is approaching (receding) knot C (B), while the stellar velocity is noncircular. Given the high gas velocity dispersion, these features indicate that the gas in knots B and C might be the complex and combined stage of collision of clouds and feedback from star formation.
- Highly spatially resolved SFEs and sSFRs are detected toward knot B. An offset between the local peaks of H $\alpha$  and CO emission is found at the bridge of B and C, and the gas therein will provide the fuel for future star formation. Limited by the sensitivity of the observations, no significant CO is detected within

knots A and T, which show relatively high sSFRs. This suggests that the molecular gas within A and T has probably been depleted by star formation or stellar feedback.

- The peak location and distribution of [CI](1–0) is very similar to the extent of CO(1–0) emission, indicating that it could trace the same molecular gas as CO in such a dwarf merger starburst galaxy. The line ratios of [CI]/CO at the north region of knot C are about 0.5, much higher than ratios in the Milky Way and normal spiral galaxies, which is probably caused by the dissociation of CO molecules by cosmic rays and FUV photons.
- Haro 11 and the star-forming regions have similar SFEs and sSFRs to the high-*z* starburst galaxies and the clumps in nearby (U)LIRGs. The turbulent pressure and virial parameter are significantly smaller than those in the massive merger galaxy NGC 4038/4039, (U)LIRGs, and post starburst galaxies, which is probably driving the intense starburst activities in Haro 11.
- Given the high SFE, sSFR, small stellar mass, and low metallicity (1/3 Z<sub>⊙</sub>), we argue that Haro 11 is analogous to high-*z* dwarf starburst galaxies and could be the potential progenitor of the nearby less massive elliptical galaxies. Considering the deficient HI gas and the potential stellar/AGN feedback therein, we predict that star formation in Haro 11 will become quenched at  $M_* \leq 8.5 \times 10^9 M_{\odot}$  after a timescale of less than 0.2 Gyr.

In conclusion, major merger of compact dwarf galaxies can induce starburst activities, which will efficiently consume the molecular gas therein. This can shed light on the mechanisms driving starbursts and quenching in less massive galaxies. Multi-band observations of ionized and molecular gas for such galaxies are need to perform a statistical analysis.

*Acknowledgements.* We thank the referee Dr. Katie Jameson for thoughtful comments and insightful suggestions that improve our paper greatly. We thank Drs. Guilin Liu, Xu Kong and Xianzhong Zheng for fruitful discussions and advice. This work is supported by the National Key Research and Development Program of China (No. 2017YFA0402703), and by the National Natural Science Foundation of China (Nos. 11733002, 12121003, 12192220, and 12192222). We also acknowledge the science research grants from the China Manned Space Project with No. CMS-CSST-2021-A05. Y.L.G. acknowledges the grant from the National Natural Science Foundation of China (No. 12103023). Z.Y.Z. acknowledges the support of NSFC (grants No. 12041305, 12173016), and the Program for Innovative Talents, Entrepreneur in Jiangsu. M.H. is fellow of the Kunt & Alice Wallenberg foundation. This paper makes use of the following ALMA data: ADS/JAO.ALMA# 2013.1.00350.S and 2017.1.01457.S. ALMA is a partnership of ESO (representing its member states), NSF (USA), and NINS (Japan), together with NRC (Canada) and NSC and ASIAA (Taiwan), in cooperation with the Republic of Chile. The Joint ALMA Observatory is operated by ESO, AUI/NRAO, and NAOJ. The National Radio Astronomy Observatory is a facility of the National Science Foundation operated under cooperative agreement by Associated Universities, Inc. This research has made use of the NASA/IPAC Extragalactic Database (NED), which is funded by the National Aeronautics and Space Administration and operated by the California Institute of Technology.

## References

- Adamo, A., Östlin, G., Zackrisson, E., et al. 2010, *MNRAS*, 407, 870  
 Alexander, D. M., Smail, I., Bauer, F. E., et al. 2005, *Nature*, 434, 738  
 Allende Prieto, C., Lambert, D. L., & Asplund, M. 2001, *ApJ*, 556, L63  
 Armus, L., Mazzarella, J. M., Evans, A. S., et al. 2009, *PASP*, 121, 559  
 Bacon, R., Accardo, M., & Adjali, L. 2010, in *Ground based and Airborne Instrumentation for Astronomy III*, eds. I. S. McLean, S. K. Ramsay, & H. Takami (Bellingham: SPIE), SPIE Conf. Ser., 7735  
 Barnes, A. T., Longmore, S. N., Dale, J. E., et al. 2020, *MNRAS*, 498, 4906  
 Bell, E. F., McIntosh, D. H., Katz, N., & Weinberg, M. D. 2003, *ApJS*, 149, 289  
 Bigiel, F., Leroy, A., Walter, F., et al. 2008, *AJ*, 136, 2846  
 Bisbas, T. G., van Dishoeck, E. F., Papadopoulos, P. P., et al. 2017, *ApJ*, 839, 90  
 Bolatto, A. D., Wolfire, M., & Leroy, A. K. 2013, *ARA&A*, 51, 207  
 Brinchmann, J., Charlot, S., White, S. D. M., et al. 2004, *MNRAS*, 351, 1151

- Brisbin, D., Miettinen, O., Aravena, M., et al. 2017, *A&A*, 608, A15
- Bruzual, G., & Charlot, S. 2003, *MNRAS*, 344, 1000
- Calzetti, D., Armus, L., Bohlin, R. C., et al. 2000, *ApJ*, 533, 682
- Catinella, B., Schiminovich, D., Kauffmann, G., et al. 2010, *MNRAS*, 403, 683
- Catinella, B., Schiminovich, D., Kauffmann, G., et al. 2012, *A&A*, 544, A65
- Catinella, B., Schiminovich, D., Cortese, L., et al. 2013, *MNRAS*, 436, 34
- Chabrier, G. 2003, *PASP*, 115, 763
- Chen, Z., He, Z., Ho, L. C., et al. 2022, *Nat. Astron.*, 6, 339
- Cheung, E., Athanassoula, E., Masters, K. L., et al. 2013, *ApJ*, 779, 162
- Cheung, E., Bundy, K., Cappellari, M., et al. 2016, *Nature*, 533, 504
- Cid Fernandes, R., Mateus, A., Sodré, L., Stasińska, G., & Gomes, J. M. 2005, *MNRAS*, 358, 363
- Cormier, D., Leboutteiller, V., Madden, S. C., et al. 2012, *A&A*, 548, A20
- Cormier, D., Madden, S. C., Leboutteiller, V., et al. 2014, *A&A*, 564, A121
- Cormier, D., Abel, N. P., Hony, S., et al. 2019, *A&A*, 626, A23
- Daddi, E., Dickinson, M., Morrison, G., et al. 2007, *ApJ*, 670, 156
- da Silva, R. L., Fumagalli, E., & Krumholz, M. R. 2014, *MNRAS*, 444, 3275
- Di Matteo, T., Springel, V., & Hernquist, L. 2005, *Nature*, 433, 604
- Di Matteo, P., Combes, F., Melchior, A. L., & Semelin, B. 2007, *A&A*, 468, 61
- Díaz-García, S., Lisenfeld, U., Pérez, I., et al. 2021, *A&A*, 654, A135
- Elbaz, D., Leiton, R., Nagar, N., et al. 2018, *A&A*, 616, A110
- Ellison, S. L., Patton, D. R., Simard, L., & McConnachie, A. W. 2008, *AJ*, 135, 1877
- Elmegreen, B. G., Galliano, E., & Alloin, D. 2009, *ApJ*, 703, 1297
- Emsellem, E., Renaud, F., Bournaud, F., et al. 2015, *MNRAS*, 446, 2468
- Espada, D., Martin, S., Verley, S., et al. 2018, *ApJ*, 866, 77
- Fabian, A. C. 2012, *ARA&A*, 50, 455
- Fang, J. J., Faber, S. M., Salim, S., Graves, G. J., & Rich, R. M. 2012, *ApJ*, 761, 23
- Fensch, J., Renaud, F., Bournaud, F., et al. 2017, *MNRAS*, 465, 1934
- Field, G. B., Blackman, E. G., & Keto, E. R. 2011, *MNRAS*, 416, 710
- Gao, Y., Lo, K. Y., Lee, S. W., & Lee, T. H. 2001, *ApJ*, 548, 172
- Geha, M., Blanton, M. R., Yan, R., & Tinker, J. L. 2012, *ApJ*, 757, 85
- Goodman, A. A., Rosolowsky, E. W., Borkin, M. A., et al. 2009, *Nature*, 457, 63
- Gratier, P., Braine, J., Rodriguez-Fernandez, N. J., et al. 2010, *A&A*, 522, A3
- Grimes, J. P., Heckman, T., Strickland, D., et al. 2007, *ApJ*, 668, 891
- Gross, A. C., Prestwich, A., & Kaaret, P. 2021, *MNRAS*, 505, 610
- Harrison, C. M., Costa, T., Tadhunter, C. N., et al. 2018, *Nat. Astron.*, 2, 198
- Hayes, M., Östlin, G., Atek, H., et al. 2007, *MNRAS*, 382, 1465
- Hayes, M., Östlin, G., Schaerer, D., et al. 2013, *ApJ*, 765, L27
- Haynes, M. P., Giovanelli, R., Kent, B. R., et al. 2018, *ApJ*, 861, 49
- He, Z., Wang, T., Liu, G., et al. 2019, *Nat. Astron.*, 3, 265
- He, Z., Liu, G., Wang, T., et al. 2022, *Sci. Adv.*, 8, eabk3291
- Heckman, T. M., Sembach, K. R., Meurer, G. R., et al. 2001, *ApJ*, 558, 56
- Heckman, T. M., Hoopes, C. G., Seibert, M., et al. 2005, *ApJ*, 619, L35
- Herrera-Camus, R., Sturm, E., Graciá-Carpio, J., et al. 2018, *ApJ*, 861, 95
- Heyer, M. H., Carpenter, J. M., & Snell, R. L. 2001, *ApJ*, 551, 852
- Hopkins, P. F., & Quataert, E. 2010, *MNRAS*, 407, 1529
- Hopkins, P. F., Hernquist, L., Cox, T. J., et al. 2006, *ApJS*, 163, 1
- Hopkins, P. F., Cox, T. J., Kereš, D., & Hernquist, L. 2008, *ApJS*, 175, 390
- Hunt, L. K., Testi, L., Casasola, V., et al. 2014, *A&A*, 561, A49
- Hunt, L. K., García-Burillo, S., Casasola, V., et al. 2015, *A&A*, 583, A114
- Hunter, D. A., Ficut-Vicas, D., Ashert, T., et al. 2012, *AJ*, 144, 134
- Hunter, D. A., Elmegreen, B. G., & Berger, C. L. 2019, *AJ*, 157, 241
- Huško, F., Lacey, C. G., & Baugh, C. M. 2022, *MNRAS*, 509, 5918
- Ikedá, M., Oka, T., Tatematsu, K., Sekimoto, Y., & Yamamoto, S. 2002, *ApJS*, 139, 467
- Israel, F. P., Rosenberg, M. J. F., & van der Werf, P. 2015, *A&A*, 578, A95
- James, B. L., Tsamis, Y. G., Walsh, J. R., Barlow, M. J., & Westmoquette, M. S. 2013, *MNRAS*, 430, 2097
- Jiao, Q., Zhao, Y., Zhu, M., et al. 2017, *ApJ*, 840, L18
- Jiao, Q., Zhao, Y., Lu, N., et al. 2019, *ApJ*, 880, 133
- Kado-Fong, E., Greene, J. E., Greco, J. P., et al. 2020, *AJ*, 159, 103
- Kauffmann, G., Heckman, T. M., Budavári, T., et al. 2007, *ApJS*, 173, 357
- Kauffmann, J., Pillai, T., & Goldsmith, P. F. 2013, *ApJ*, 779, 185
- Kaviraj, S., Laigle, C., Kimm, T., et al. 2017, *MNRAS*, 467, 4739
- Kennicutt, R. C., Jr 1998, *ApJ*, 498, 541
- Kennicutt, R. C., Jr, Calzetti, D., Walter, F., et al. 2007, *ApJ*, 671, 333
- Kennicutt, R. C., & Evans, N. J. 2012, *ARA&A*, 50, 531
- Knobel, C., Lilly, S. J., Woo, J., & Kovač, K. 2015, *ApJ*, 800, 24
- Kormendy, J., & Kennicutt, R. C., Jr 2004, *ARA&A*, 42, 603
- Krieger, N., Bolatto, A. D., Koch, E. W., et al. 2020, *ApJ*, 899, 158
- Krips, M., Martín, S., Sakamoto, K., et al. 2016, *A&A*, 592, L3
- Kroupa, P. 2001, *MNRAS*, 322, 231
- Krumholz, M. R., & McKee, C. F. 2005, *ApJ*, 630, 250
- Kunth, D., & Östlin, G. 2000, *A&ARv.*, 10, 1
- Lahén, N., Johansson, P. H., Rantala, A., Naab, T., & Frigo, M. 2018, *MNRAS*, 475, 3934
- Larson, R. B., & Tinsley, B. M. 1978, *ApJ*, 219, 46
- Larson, K. L., Sanders, D. B., Barnes, J. E., et al. 2016, *ApJ*, 825, 128
- Leroy, A. K., Walter, F., Brinks, E., et al. 2008, *AJ*, 136, 2782
- Li, C., Wang, H.-C., Wu, Y.-W., Ma, Y.-H., & Lin, L.-H. 2020, *Res. Astron. Astrophys.*, 20, 031
- Lilly, S. J., Carollo, C. M., Pipino, A., Renzini, A., & Peng, Y. 2013, *ApJ*, 772, 119
- Madden, S. C. 2000, *New Astrom. Rev.*, 44, 249
- Madden, S. C., Poglitsch, A., Geis, N., Stacey, G. J., & Townes, C. H. 1997, *ApJ*, 483, 200
- Madden, S. C., Rémy-Ruyer, A., Galametz, M., et al. 2013, *PASP*, 125, 600
- Madden, S. C., Cormier, D., Hony, S., et al. 2020, *A&A*, 643, A141
- Marino, R. A., Rosales-Ortega, F. F., Sánchez, S. F., et al. 2013, *A&A*, 559, A114
- Masters, K. L., Nichol, R. C., Hoyle, B., et al. 2011, *MNRAS*, 411, 2026
- McMullin, J. P., Waters, B., Schiebel, D., Young, W., & Golap, K. 2007, in *Astronomical Data Analysis Software and Systems XVI*, eds. R. A. Shaw, F. Hill, & D. J. Bell, (San Francisco: ASP), ASP Conf. Ser., 376, 127
- Menacho, V., Östlin, G., Bik, A., et al. 2019, *MNRAS*, 487, 3183
- Menacho, V., Östlin, G., Bik, A., et al. 2021, *MNRAS*, 506, 1777
- Murray, N. 2011, *ApJ*, 729, 133
- Narayanan, D., Hayward, C. C., Cox, T. J., et al. 2010, *MNRAS*, 401, 1613
- Oka, T., Hasegawa, T., Sato, F., et al. 2001, *ApJ*, 562, 348
- Orlitova, I. 2020, ArXiv e-prints, [arxiv:2012.12378v1].
- Östlin, G., Hayes, M., Duval, F., et al. 2014, *ApJ*, 797, 11
- Östlin, G., Marquart, T., Cumming, R. J., et al. 2015, *A&A*, 583, A55
- Östlin, G., Rivera-Thorsen, T. E., Menacho, V., et al. 2021, *ApJ*, 912, 155
- Papadopoulos, P. P., Isaak, K. G., & van der Werf, P. P. 2007, *ApJ*, 668, 815
- Papadopoulos, P. P., Bisbas, T. G., & Zhang, Z.-Y. 2018, *MNRAS*, 478, 1716
- Pardy, S. A., Cannon, J. M., Östlin, G., Hayes, M., & Bergvall, N. 2016, *AJ*, 152, 178
- Paudel, S., Smith, R., Yoon, S. J., Calderón-Castillo, P., & Duc, P.-A. 2018, *ApJS*, 237, 36
- Peng, Y.-J., Lilly, S. J., Kovač, K., et al. 2010, *ApJ*, 721, 193
- Peng, Y., Maiolino, R., & Cochrane, R. 2015, *Nature*, 521, 192
- Rémy-Ruyer, A., Madden, S. C., Galliano, F., et al. 2013, *A&A*, 557, A95
- Rémy-Ruyer, A., Madden, S. C., Galliano, F., et al. 2015, *A&A*, 582, A121
- Renzini, A., & Peng, Y.-J. 2015, *ApJ*, 801, L29
- Rodriguez-Gomez, V., Snyder, G. F., Lotz, J. M., et al. 2019, *MNRAS*, 483, 4140
- Romano, M., Cassata, P., Morselli, L., et al. 2021, *A&A*, 653, A111
- Saintonge, A., Catinella, B., Cortese, L., et al. 2016, *MNRAS*, 462, 1749
- Shangguan, J., Ho, L. C., Li, R., et al. 2019, *ApJ*, 870, 104
- Shapiro, K. L., Genzel, R., Förster Schreiber, N. M., et al. 2008, *ApJ*, 682, 231
- Shi, Y., Helou, G., Yan, L., et al. 2011, *ApJ*, 733, 87
- Shi, Y., Wang, J., Zhang, Z.-Y., et al. 2016, *Nat. Commun.*, 7, 13789
- Shi, Y., Yan, L., Armus, L., et al. 2018, *ApJ*, 853, 149
- Shimajiri, Y., Sakai, T., Tsukagoshi, T., et al. 2013, *ApJ*, 774, L20
- Romano, A., Smith, J. D. T., Dale, D. A., et al. 2018, *ApJ*, 855, 51
- Smercina, A., Smith, J.-D. T., French, K. D., et al. 2022, *ApJ*, 929, 154
- Speagle, J. S., Steinhardt, C. L., Capak, P. L., & Silverman, J. D. 2014, *ApJS*, 214, 15
- Spence, R. A. W., Tadhunter, C. N., Rose, M., & Rodríguez Zaurín, J. 2018, *MNRAS*, 478, 2438
- Sternberg, A., Le Petit, F., Roueff, E., & Le Bourlot, J. 2014, *ApJ*, 790, 10
- Sternberg, A., Gurman, A., & Bialy, S. 2021, *ApJ*, 920, 83
- Stierwalt, S., Armus, L., Surace, J. A., et al. 2013, *ApJS*, 206, 1
- Stierwalt, S., Besla, G., Patton, D., et al. 2015, *ApJ*, 805, 2
- Sun, J., Leroy, A. K., Schrubba, A., et al. 2018, *ApJ*, 860, 172
- Tacconi, L. J., Neri, R., Genzel, R., et al. 2013, *ApJ*, 768, 74
- Taft, S., Cannon, J. M., & Pardy, S. 2019, *Am. Astron. Soc. Meet.*, 233, 368.10
- Tanaka, K., Oka, T., Matsumura, S., Nagai, M., & Kamegai, K. 2011, *ApJ*, 743, L39
- Tremonti, C. A., Heckman, T. M., Kauffmann, G., et al. 2004, *ApJ*, 613, 898
- Tsuge, K., Fukui, Y., Tachihara, K., et al. 2021, *PASJ*, 73, S35
- Vader, J. P., Frogel, J. A., Terndrup, D. M., & Heisler, C. A. 1993, *AJ*, 106, 1743
- Wardlow, J. L., Cooray, A., Osage, W., et al. 2017, *ApJ*, 837, 12
- Weigel, A. K., Schawinski, K., Caplar, N., et al. 2017, *ApJ*, 845, 145
- Whitney, A., Ferreira, L., Conselice, C. J., & Duncan, K. 2021, *ApJ*, 919, 139
- Wilson, C. D., Warren, B. E., Israel, F. P., et al. 2009, *ApJ*, 693, 1736
- Wilson, C. D., Elmegreen, B. G., Bemis, A., & Brunetti, N. 2019, *ApJ*, 882, 5
- Wolfire, M. G., Hollenbach, D., & McKee, C. F. 2010, *ApJ*, 716, 1191
- Zhang, H.-X., Paudel, S., Smith, R., et al. 2020a, *ApJ*, 891, L23
- Zhang, H.-X., Smith, R., Oh, S.-H., et al. 2020b, *ApJ*, 900, 152